Acta Geologica Sinica (English Edition), 2019, 93(4): 820–844

Early Carboniferous High Ba-Sr Granitoid in Southern Langshan of Northeastern Alxa: Implications for Accretionary Tectonics along the Southern Central Asian Orogenic Belt

ZHENG Rongguo[1, 2, *], LI Jinyi[1], ZHANG Jin[1], XIAO Wenjiao[2, 3, 4, 5] and LI Yi[6]

[1] *Institute of Geology, Chinese Academy of Geological Sciences, Beijing 100037, China*
[2] *Xinjiang Research Center for Mineral Resources, Xinjiang Institute of Ecology and Geography, ChineseAcademy of Sciences, Urumqi 830011, China*
[3] *State Key Laboratory of Lithospheric Evolution, Institute of Geology and Geophysics, Chinese Academy of Sciences, Beijing 100029, China*
[4] *CAS Center for Excellence in Tibetan Plateau Earth Science, Chinese Academy of Sciences, Beijing100101, China*
[5] *University of Chinese Academy of Sciences, Beijing 100049, China*
[6] *China Minmetals Corporation, Beijing 100010, China*

Abstract: Voluminous granitoids are widely distributed in the Langshan region, northeast of the Alxa block, and record the evolutionary processes of the southern Central Asian Orogenic Belt. The Dabashan pluton was emplaced into the Paleoproterozoic Diebusige complex. Early Carboniferous zircon LA-ICP MS U-Pb ages were from 327 Ma to 346 Ma. The Dabashan pluton can be classified as monzogranite and syenogranite, and exhibits high K_2O contents and K_2O/Na_2O ratios, which reveal a high-K calc-alkaline nature. The samples display strongly fractionated REE patterns, and are enriched in large ion lithophile elements (LILE) relative to high field strength elements (HFSE). The Dabashan plutons display unusually high Ba (823–2817 ppm) and Sr (166–520 ppm) contents and K/Rb ratios (315–627), but low Rb/Ba ratios (0.02–0.14), and exhibit fertile zircon Hf isotopic compositions [$\varepsilon_{Hf}(t)$=−14 to −20], which are comparable to those of typical high Ba–Sr granitoids. Based on the geochemical compositions of the samples, we suggest that subducted sediments and ancient crustal materials both played important roles in their generation. Basaltic melts were derived from partial melting of subcontinental lithophile mantle metasomatized by subducted sediment-related melts with residual garnet in the source, which caused partial melting of ancient lower crust. Magmas derived from underplating ascended and emplaced in the middle–upper crust at different depths. The resultant magmas experienced some degree of fractional crystallization during their ascent. Given these geochemical characteristics, together with regional tectonic, magmatic, and structure analysis data, an active continental margin environment is proposed for the generation of these rocks .

Key words: LA–ICP MS U–Pb, Zircon Hf isotope, high Ba–Sr granites, CAOB, Alxa

Citation: Zheng et al., 2019. Early Carboniferous High Ba-Sr Granitoid in Southern Langshan of Northeastern Alxa: Implications for Accretionary Tectonics along the Southern Central Asian Orogenic Belt. Acta Geologica Sinica (English Edition), 93(4): 820–844. DOI: 10.1111/1755-6724.13803

1 Introduction

Granitoids, as a main component of the continental crust, carry important clues to better understand the tectonics and geological evolution of the continental crust (Zhang et al., 2016; Zhang et al., 2017). Probing the origins and emplacement processes of granitoids is crucial for understanding continental crustal growth and crustal evolution. A great deal of geological and geophysical evidence has demonstrated that crustal sediments may be transported by subducted channels into the mantle (Su et al., 2017); large amounts of sediments could thus be brought into subduction zones. Partial melting of subducted oceanic sediments could generate felsic magmas that intrude the overlying crustal material as granitoid plutons (Ishizuka et al., 2003; Spandler and Pirard, 2013; Zhang et al., 2016). Such subduction-related granitoids exhibit crust-like major- and trace-elemental compositions and radiogenic isotope ratios because large components are derived from continental sediments (Sun et al., 2014; Conticelli et al., 2015; Malyshev et al., 2016; Zhang et al., 2016; Zhang et al., 2017).

The term ‘‘high Ba–Sr granite’’ was first proposed by Tarney and Jones (1994) based on the unique geochemical characteristics of these rocks. In contrast with low Ba–Sr granites, high Ba–Sr granites are characterized by high Ba and Sr contents, low Y and heavy rare earth element (HREE) abundances, and depletion of Nb in their trace element spidergrams (Tarney and Jones, 1994; Fowler et al., 2001, 2008; Qian et al., 2003; Peng et al., 2013). Because of their unique geochemical characteristics, high

* Corresponding author. E-mail: rgzheng@163.com

http://www.geojournals.cn/dzxbcn/ch/index.aspx; https://onlinelibrary.wiley.com/journal/17556724

Ba–Sr granites have drawn considerable attention. Many researchers have focused on the petrogenesis and tectonic settings of these rocks, and their associations with mineralization (e.g. Fowler et al., 2008; Ye et al., 2008; Choi et al., 2009; Peng et al., 2013; Liu et al., 2017).

The Central Asian Orogenic Belt (CAOB) is one of the largest and longest-lived accretionary orogenic collages in the world, and is located between the Siberian and Baltica cratons to the north and the Tarim and North China cratons to the south (Fig. 1a; Sengör et al., 1993; Jahn et al., 2000; Kovalenko et al., 2004; Windley et al., 2007; Xiao et al., 2015, 2018). There is a general consensus that the CAOB grew by successive lateral accretion of arcs, accretionary complexes, and a few continental blocks southward from Siberia and southern Mongolia during the evolution of the Paleo-Asian Ocean (Windley et al., 2007; Xiao et al., 2015, 2018). Thus, the CAOB was largely formed by subduction and accretion of juvenile material from the Neoproterozoic through the end of the Paleozoic (Jahn et al., 2000; Windley et al., 2007; Xiao et al., 2015, 2018). Paleozoic granitoids are widely distributed in the CAOB, and record the long-lived evolutionary history and Phanerozoic crustal growth of this region.

The Alxa block and its peripheral regions were involved in Paleozoic orogeny during the evolution of the Paleo-Asian Ocean (PAO), and are key to depicting the architecture of the central segment of the southernmost of CAOB. Late Paleozoic granitic plutons are widely exposed in the Alxa block and its peripheral regions, and clearly record important information on the evolution of the PAO. For example, zircon U-Pb age data show that late Paleozoic plutons with age peaks of 278 Ma, 270 Ma, and 248 Ma (Zheng et al., 2016) are widely distributed at the northern margin of the Alxa block. In the Alxa Youqi region, west of the Alxa block, late Paleozoic to Mesozoic magmatic rocks are predominant, including voluminous 418–239 Ma granitoids and minor 328–249 Ma gabbro-diorites (e.g., Liu et al., 2016b and references therein).

The Langshan region, located in the northeast of the Alxa block, is a junctional zone between the CAOB, the Alxa block, and the North China Craton (NCC) (Fig. 1b). Recent studies found various Paleozoic (mainly late Paleozoic) plutons widely exposed in the Langshan region (Wang et al., 2015; Dan et al., 2016; Liu et al., 2016a),

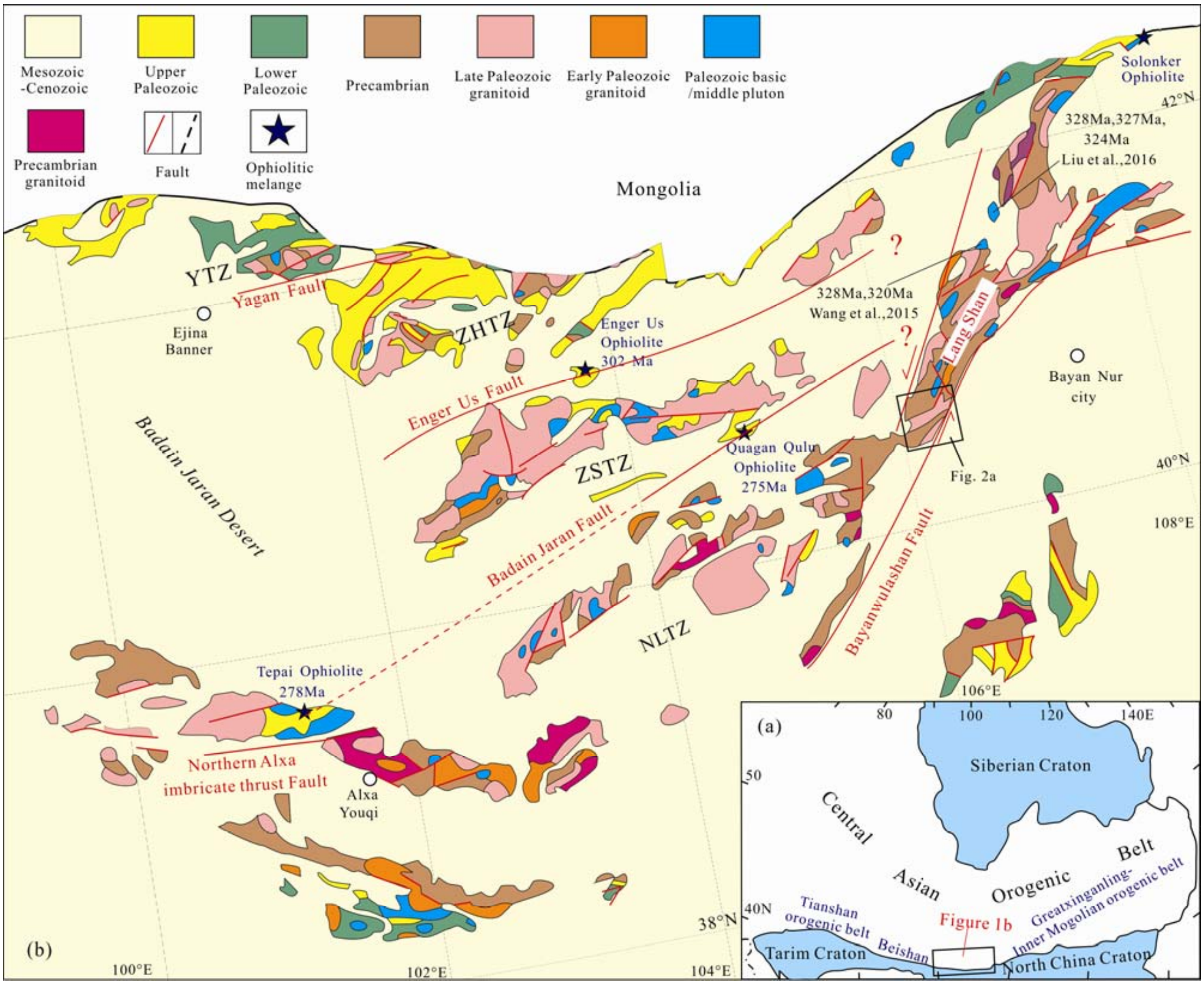

Fig. 1. (a) Geological sketch map of Central Asian Orogenic Belt (modified from Şengör et al., 1993; Jahn et al., 2000); (b) Geological map of Alxa region (modified from Zheng et al., 2014; YTZ, Yagan tectonic zone; ZHTZ, Zhusileng-Hangwula tectonic zone; ZSTZ, Zongnaishan-Shalazhashan tectonic zone; NLTZ, Nuoergong-Langshan tectonic zone).

indicating long-lived and complex magmatic activities. These Paleozoic plutons could help us to recognize the Paleozoic tectonic history of the PAO in the northeast of the Alxa region. However, the tectonic implications and petrogenesis of these plutons are still debated because of a lack of detailed geochronological and geochemical work.

In this study, we report new zircon U–Pb ages, bulk-rock major and trace element, and zircon Hf isotopic data for the Dabashan pluton in southern Langshan. Based on our data, together with previously published data, we attempt to track the petrogenesis of these plutons, provide important constraints on the tectonic setting, and compare them with coeval plutons in the northern margin of the NCC.

2 Geological Background

The Alxa block is located to the south of the CAOB (Fig. 1a), and is traditionally regarded as one component of the western block of the NCC, such as the extension of the Yinshan Block (Zhao et al., 2005) or the Khondalite Belt (Dong et al., 2007; Geng et al., 2010; Zhang et al., 2013b). However, some researchers have proposed that the Alxa block may be an independent Paleoproterozoic terrane, and might have amalgamated to the NCC during the Phanerozoic (Zhang et al., 2012; Li et al., 2012; Lin et al., 2014; Yuan and Yang, 2015; Xiao et al., 2015, 2018; Dan et al., 2016).

Paleozoic strata and magmatic deposits are widespread in the Alxa block and its peripheral regions because of the influence of the PAO. Two late Paleozoic ophiolitic mélanges have been reported from the northern margin of the Alxa block, and are considered fragments of the PAO (Zheng et al., 2014). Based on the different sedimentary sequences and magmatic events during the Paleozoic, the Alxa block and its peripheral regions can be divided into four Paleozoic tectonic subunits: the Yagan tectonic zone (YTZ), the Zhusileng–Hangwulatectonic zone (ZHTZ), the Zongnaishan–Shalazhashan tectonic zone (ZSTZ), and the Nuru–Langshan tectonic zone (NLTZ) (Fig.1b, Wu and He, 1993; Zheng et al., 2014).

The NLTZ is characterized by extensive outcrops of Precambrian rocks and Paleozoic plutons (Wu and He, 1993; Zheng et al., 2014; Gong et al., 2017). Abundant late Paleozoic plutons emplaced into the Precambrian strata in the NLTZ imply that those Precambrian rocks were strongly reworked in the orogenic processes of the CAOB in the late Paleozoic (Geng and Zhou, 2012).

The Langshan region is located in the eastern segment of the NLTZ. There are a widely distributed high-grade metamorphic complex (Diebusige complex) and low-grade meta-volcanic and meta-sedimentary rocks (Langshan group) in the southern Langshan region (Fig. 2a). The Diebusige complex is mainly composed of amphibolites, mafic gneisses, paragneisses, TTG, quartzite, magnetite-quartzite, and minor marble. The depositional ages of the protoliths of the Diebusige paragneisses are estimatedto be between ca. 2.45 and 2.0 Ga (Dan et al., 2012). Protoliths of the Diebusige TTG exhibit Paleoproterozoic ages (2.41 Ga, unpublished data). The Diebusige complex was intruded by granites dated at ca. 1.97–1.98 Ga, and was subjected to high-grade metamorphic events at ca. 1.89 Ga and ca. 1.79 Ga (Dan et al., 2012). The Langshan group is located to the northwest of the Diebusige complex, and is mainly composed of low -grade meta-volcanic and meta-sedimentary rocks, such as marble, quartzite, meta-sandstone, and mica-quartzite schist, which are interpreted as a rift sequence (Lu et al., 2002). The minimum detrital zircon U–Pb ages of meta-sedimentary rocks in the Langshan group are from 810 to 1187 Ma, which indicate that these meta-sedimentary rocks were deposited in the Neoproterozoic (Hu et al., 2014). Neoproterozoic meta-volcanic rocks with zircon U–Pb ages of 804–816 Ma are also recognized in the Langshan group (Hu et al., 2014). Upper Paleozoic strata are rare, and scarce Carboniferous–Permian marine sedimentary rocks are exposed only in the west of the Langshan region (Fig. 2a).

Paleozoic plutons, including predominant granitoids, subordinate maficplutons, and minor volcanic rocks, are widely distributed in the Langshan region, mostly emplaced into Precambrian units (Fig. 2a). Most plutons exhibit late Paleozoic zircon U–Pb ages. Zircon U–Pb data from plutons in the Langshan region reveal five magmatic stages during the Paleozoic–Triassic (Wang et al., 2015 and references therein), including Late Silurian (~418 Ma), Carboniferous (328–304 Ma), Early Permian (294–272 Ma), Late Permian (260–254 Ma), and Middle–Late Triassic (245–227 Ma).

3 Sampling and Analytical Method

3.1 Sampling

The Dabashan pluton is located in the southeasternmost part of the Langshan region, emplaced into the Diebusige complex (Fig. 3a–c). In this study, we analyzed granite samples collected from six locations in the Dabashan pluton, including the series of ZH7, ZH15, Rg32, Rg40, Rg42, and Rg55 (see locations in Fig. 2b). The series of ZH7 and ZH15 were collected in the Dairigen valley. The other samples were collected in the Dabashan Mountain. In this study, we named all samples after the Dabashan pluton for short. Except series Rg40, all the other granites show strong mylonitization (Fig. 3e and f), and L-type mylonites were observed in some outcrops. Ductile sinistral shear deformation is pronounced in the Dabashan pluton. The quartz stretching lineations indicate NE-trending sinistral shearing (Fig. 3g). Except series Rg40, the other granites exhibit similar mineral compositions. Those granites display porphyritic textures with quartz porphyroblasts (Fig. 3g). They are mainly composed of plagioclase (30–40 vol%), K-feldspar (25–30 vol%), quartz (25–35 vol%), biotite (5–10 vol.%), and minor accessory minerals (Fig. 3h).The samples of the Rg40 series display yellowish-brown and massive structure. They are covered by coarse Cretaceous clastic rocks (Fig. 3d), and cut by lateral thrust faults. These samples mainly consist of plagioclase (30–40 vol%), perthite (20–30 vol%), quartz (25–35 vol%), biotite (5–10 vol%), and muscovite (2–5 vol%) (Fig. 3j).

3.2 Zircon LA-ICP-MS U–Pb dating

Zircons from crushed samples were separated by using conventional heavy liquid and magnetic techniques in the Laboratory of Langfang Regional Geological Survey, Hebei Province, China. Representative zircon grains were hand-picked under a binocular microscope, mounted in epoxy resin, polished, and coated with gold film. Zircons were photographed in transmitted and reflected light. Those photos, together with cathodoluminescence (CL) images were used to examine the external and internal structures of the analyzed zircons at the Gaonian Navigation Technology Company, Beijing, China.

Laser ablation (LA)–ICP MS zircon U-Pb geochronological dating was carried out at Key laboratory of Mineral Resources Evaluation in Northeast Asia, Ministry of Land and Resources of China. The instrument couples a quadrupole ICP-MS (Agilient 7900) and 193-nm ArF Excimer laser (COMPexPro 102, Coherent, DE) with the automatic positioning system. For the present work, laser spot size was set to 32 μm for most analyses, laser energy density at 10 J/cm^2 and repetition rate at 8 Hz. The procedure of laser sampling is 30-s blank, 30-seconds sampling ablation, and 2min- sample -chamber flushing after the ablation. The ablated material is carried into the ICP-MS by the high-purity Helium gas stream with flux of 1.15 L/min. The whole laser path was fluxed with Ar (600m L/min) in order to increase energy stability. The counting time is 20ms for ^{204}Pb, ^{206}Pb, ^{207}Pb and ^{208}Pb, 15ms for ^{232}Th, ^{238}U, 20 ms for ^{49}Ti, and 6 ms for other elements. Calibrations for the zircon analyses were carried out using NIST 610 glass as an external standard and Si as internal standard. U–Pb isotope fractionation effects were corrected using zircon 91500 (Wiedenbeck et al., 1995) as external standard. Zircon standard Plesovice (337 Ma) is also used as a secondary standard to supervise the deviation of age measurement/ calculation (Sláma, et al., 2008). Isotopic ratios and element concentrations of zircons were calculated using Glitter. Concordia ages and diagrams were obtained using Isoplot/Ex (3.0) (Ludwig,

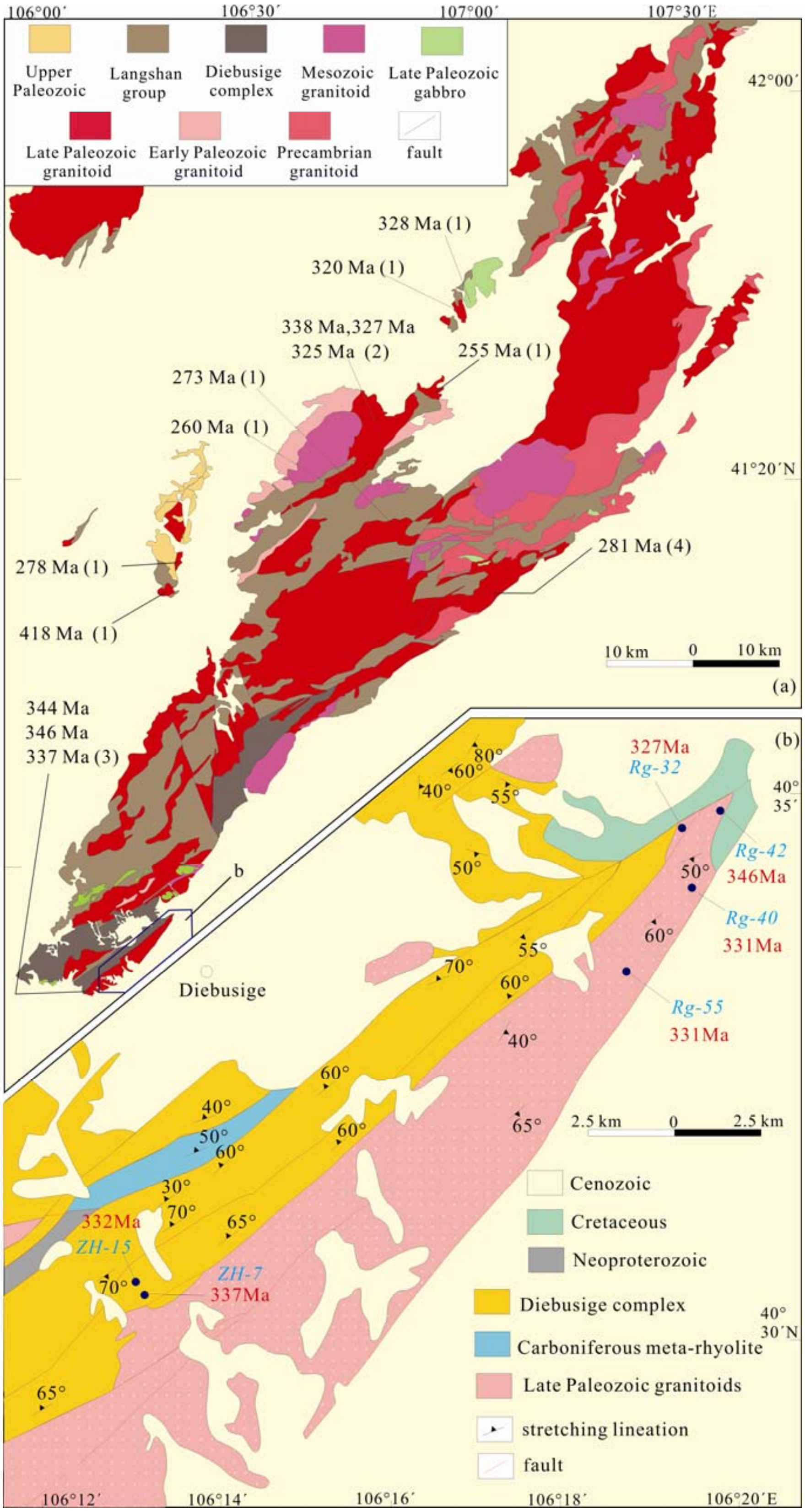

Fig. 2. (a) Geological map of the Langshan region, showing distributions of Paleozoic plutons. Sources of age data: (1) Wang et al., 2015; (2) Liu et al., 2016a; (3) Dan et al., 2016; (4) Lin et al., 2014; (b) geological map of the southern Langshan, showing locations of samples and their zircon U-Pb data.

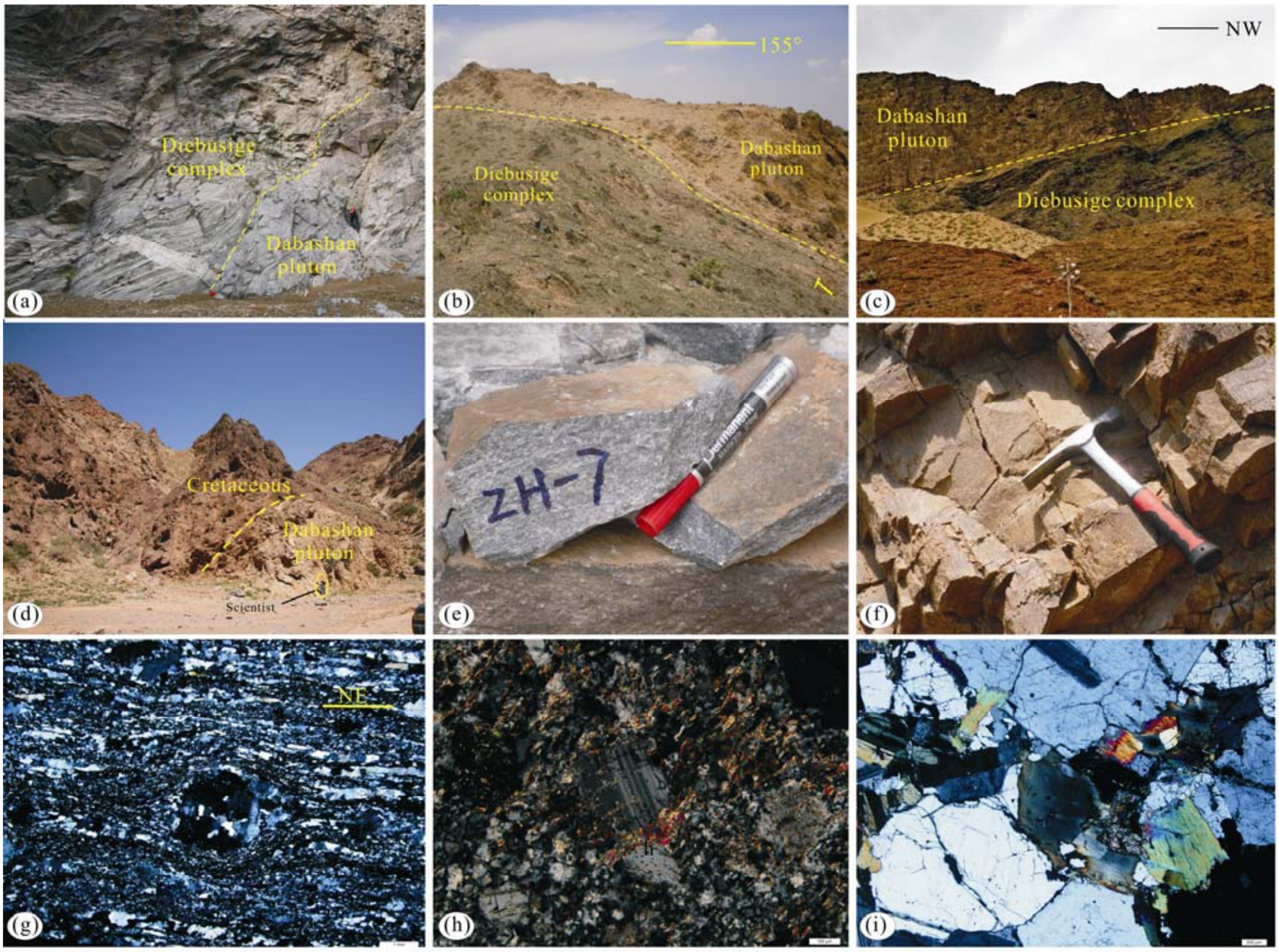

Fig. 3. Field photos of Dabshan pluton, showing typical lithologies and structures.
(a) Dabashan pluton intruded into Diebusige complex in the Dairigen valley; (b) and (c) Dabashan pluton emplaced into the Diebusige complex; (d) Dabashan pluton were overlain by the Cretaceous; (e) and (f) typical outcrops of the Dabashan pluton; (g) and (h) mineral compositions of the mylonitized granites from Dabshan pluton; (j) mineral compositions of the unformed granites from Dabshan pluton.

2003). The common lead was corrected using LA-ICP-MS Common Lead Correction (ver. 3.15), followed the method of Andersen (2002). The analytical data are presented on U-Pb Concordia diagrams with 2σ errors. The mean ages are weighted means at 95% confidence levels (Ludwig, 2003).

3.3 Major and trace elemental analyses

Whole-rock major and trace element compositions were analyzed at the Analytical Laboratory of the CNNC Beijing Research Institute of Uranium Geology (BRIUG), China. Major element compositions were determined by XRF (Philips PW2404), and the analytical precision was within 1%. The trace element compositions analysis was conducted by following the technique of Li (1997). Approximately 50 mg of each sample was dissolved in high-pressure Teflon beakers by using a $HF+HNO_3$ mixture. The solutions were centrifuged after dissolution, and the supernatants were moved to clean Teflon beakers. The solutions were evaporated to near dryness and then added 1.0 ml concentrated HNO_3 and dried twice to eliminate the influence of the HF or HCl. Afterward, all the analyzed samples were dissolved in 5% HNO_3 solution with an internal standard Rh for analysis. The trace element compositions were analyzed by using a PerkinElmer ELAN DRC-e inductively coupled plasma mass spectrometer (ICP-MS) and the analytical uncertainties were mostly better than 5%.

3.4 In situ zircon Hf isotopic analyses

Zircon Hf isotope was analyzed in the Continental Tectonics and Dynamics Laboratory of Institute of Geology, Chinese Academy of Geological Sciences. The instruments used in the analysis were one Neptune Plus Multiple Receiving Plasma Mass Spectrometer and Compex pro.193 nm UV laser ablation system (LA-MC-ICP-MS). During the experiment, Helium was used as the carrier gas to bring denudation substance. According to zircon size, ablation diameter was 44 μm or 32 μm. A common international accepted zircon standard sample GJ -1 was used as a reference material in the experiment. The analysis spots are the same spots for the U-Pb dating. Related conditions for the instruments operation and a detailed analysis procedure can be found in ref. Hou Kejun et al (2007). Weighted average analysis result of $^{176}Hf/^{177}Hf$ was 0.282015±8 (2σ, n=10) in the zircon standard sample GJ1, which was coincided exactly with the reported values (Hou Kejun et al, 2007) within the identical error.

4. Result

4.1 Zircon U–Pb geochronological and Hf isotopic compositions

Represented CL images of zircons are presented in Fig. 4. The U–Pb dating results are listed in the Table 1, and presented as concordia diagrams (Fig. 5). Zircon Lu–Hf isotopes were also analyzed for dating samples from those plutons, with corresponding U–Pb dating on the same or similar domains. The analytical results are listed in the Table 2. The $\varepsilon_{Hf}(t)$ values and model ages are calculated using their $^{206}Pb/^{238}U$ ages.

In general, the majority of zircon grains from the Dabashan pluton in the southern Langshan have a rather simple morphology of magmatic origin. Those dated zircon grains are euhedral and prismatic, and most zircons show obvious oscillatory or planar zoning in the CL images (Fig. 4), which are typical features of magmatic zircons. Zircons have variable Th and U concentrations, but the majority of these are lower than 500 ppm (Table 1). The Th/U ratios of dating zircons vary between 0.02 and 0.75, and the majority are higher than 0.1 (Table 1). All these features are consistent with the zircons having a magmatic origin.

4.1.1 Sample ZH7–1

Thirty grain zircons were selected from the sample (ZH7–1) for U-Pb analysis. Two analyses exhibit relatively old $^{206}Pb/^{238}U$ apparent ages (369 Ma and 376 Ma), which may be inherited zircons. The other 28 analyses yield close $^{206}Pb/^{238}U$ apparent ages of 332–344 Ma, with a weighted mean age of 336.5±1.9 Ma (MSWD=0.18, n=28, Fig. 5a), which is interpreted as the crystallization age.

4.1.2 Sample ZH15–1

Sixty spots were analyzed for sample ZH15–1. Eleven inherited zircons exhibit relatively old $^{206}Pb/^{238}U$ apparent ages, and form two tight clusters in the Concordia diagram with weighted mean ages of 369±6 Ma and 345±4 Ma, respectively. The other forty-nine analyses yield close $^{206}Pb/^{238}U$ apparent ages of 330–339 Ma, with a weighted mean age of 332.2±1.4 Ma (MSWD=0.031, n=49, Fig. 5b), which is interpreted as the crystallization age. 21 zircon grains from sample ZH15–1 were analyzed to obtain their Lu–Hf isotopic compositions. The $(^{176}Hf/^{177}Hf)_i$ ratios vary from 0.282038 to 0.282130. All zircon grains exhibit negative $\varepsilon_{Hf}(t)$ values, varying from −15.42 to −17.81 (Fig. 6b), and relatively old T_{DM2} model ages, ranging from 2.46 to 2.51 Ga.

4.1.3 Sample Rg32–1

Twenty-eight zircon grains were selected from sample Rg32–1 for U–Pb analysis. Five analyses exhibit relatively old $^{206}Pb/^{238}U$ apparent ages (347 Ma–3363 Ma), which may be inherited zircons. The other 23 analyses with colse $^{206}Pb/^{238}U$ apparent ages give a weighted mean age of 327.1±2.0 Ma (MSWD=0.018, n=23, Fig. 5c), which is interpreted as the crystallization age. 21 zircon grains from sample Rg-32 were analyzed to obtain their Lu–Hf isotopic compositions. The $(^{176}Hf/^{177}Hf)_i$ ratios vary from 0.282001 to 0.282147. All zircon grains exhibit negative $\varepsilon_{Hf}(t)$ values, varying from −14.97 to −0.08 (Fig. 6b), and relatively old T_{DM2} model ages, ranging from 2.27 to 2.60 Ga.

4.1.4 Sample Rg40–5

Thirty zircon spot analyses from sample Rg40–5 show a wide range of $^{206}Pb/^{238}U$ ages varying from 329 Ma to

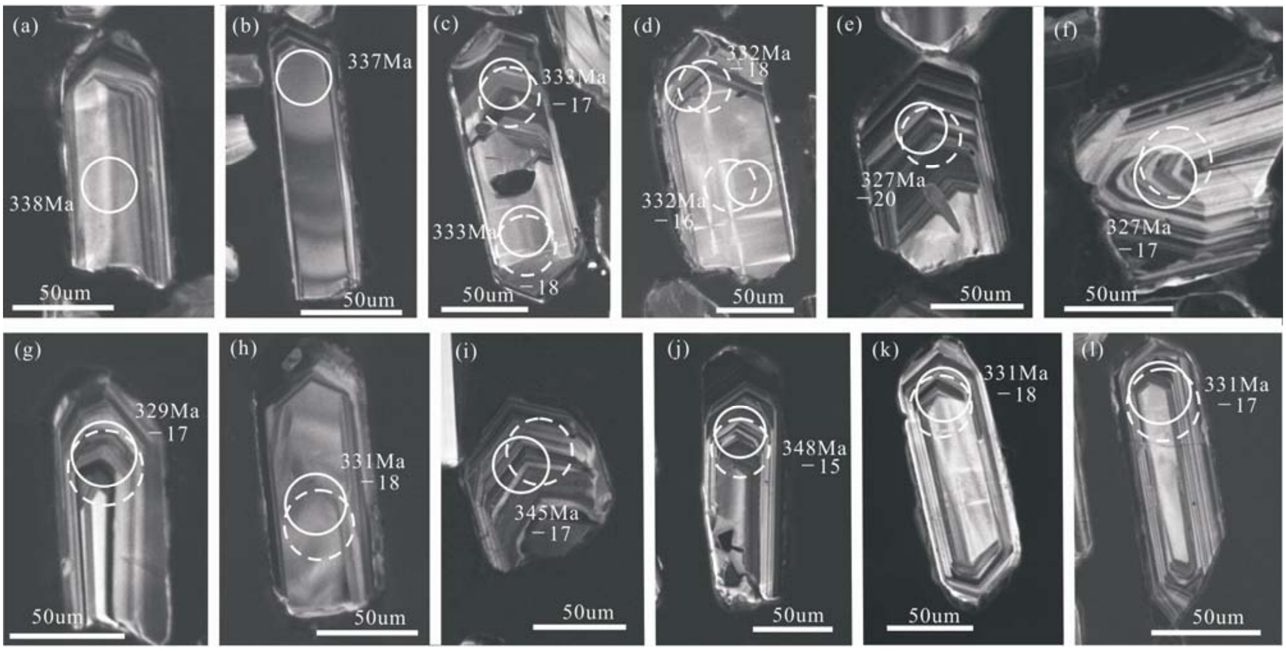

Fig. 4. Representative cathodoluminescence (CL) images of zircons from Dabashan pluton in the southern Langshan.

The circles with yellow solid lines for U–Pb analysis points and the circles with red dash lines for Hf isotope analysis points; The yellow and red numbers represent $^{206}Pb/^{238}U$ ages and $\varepsilon_{Hf}(t)$ values, respectively.

Table 1 Zircon U–Pb analytical data of Dabashan pluton in the southern Langshan

Spots	^{238}U (ppm)	^{232}Th (ppm)	^{232}Th/^{238}U	Ratio						Age					
				^{207}Pb*/^{206}Pb*		^{207}Pb*/^{235}U		^{206}Pb*/^{238}U		^{207}Pb*/^{206}Pb*		^{207}Pb*/^{235}U		^{206}Pb*/^{238}U	
				ratio	±%	ratio	±%	ratio	±%	age	1σ	age	1σ	age	1σ
ZH7-1, Syenogranite: weighted mean age: 336.5±1.9 Ma, n=28, (MSWD = 0.18)															
1	162.3	34.7	0.21	0.05382	0.00112	0.39897	0.00675	0.05376	0.00086	364	17	341	5	338	5
2	116.5	17.7	0.15	0.05402	0.00144	0.43892	0.01029	0.05892	0.00097	372	26	369	7	369	6
3	105.1	11.4	0.11	0.06249	0.0016	0.46039	0.00928	0.05343	0.00085	691	56	385	6	336	5
4	138.3	31.3	0.23	0.05377	0.00115	0.39839	0.00698	0.05373	0.00086	361	18	340	5	337	5
5	114.3	12.9	0.11	0.0534	0.00119	0.3954	0.00735	0.0537	0.00086	346	19	338	5	337	5
6	63.6	6.8	0.11	0.05266	0.00155	0.38803	0.00957	0.05344	0.00085	314	68	333	7	336	5
7	116.2	17.4	0.15	0.05293	0.00149	0.39041	0.00905	0.05349	0.00085	326	65	335	7	336	5
8	174.4	12.5	0.07	0.0622	0.00192	0.45738	0.01198	0.05333	0.00087	681	67	382	8	335	5
9	70.7	2.8	0.04	0.06246	0.00161	0.45673	0.00932	0.05303	0.00084	690	56	382	6	333	5
10	122.8	17.5	0.14	0.05639	0.00147	0.4183	0.00869	0.0538	0.00085	468	59	355	6	338	5
11	100.8	10.2	0.10	0.05697	0.00155	0.42108	0.00926	0.0536	0.00085	490	61	357	7	337	5
12	115.6	18.6	0.16	0.05411	0.0013	0.40197	0.00824	0.05386	0.00087	376	21	343	6	338	5
13	81.0	13.6	0.17	0.0631	0.00172	0.4653	0.01027	0.05348	0.00085	712	59	388	7	336	5
14	92.7	14.8	0.16	0.06171	0.00192	0.45644	0.01214	0.05364	0.00087	664	68	382	8	337	5
15	326.1	245.8	0.75	0.05368	0.00125	0.39641	0.00781	0.05355	0.00086	358	20	339	6	336	5
16	121.0	15.6	0.13	0.05332	0.00164	0.39393	0.01095	0.05358	0.0009	342	34	337	8	336	6
17	118.8	17.1	0.14	0.06078	0.00179	0.44714	0.01102	0.05336	0.00086	631	65	375	8	335	5
18	136.9	20.0	0.15	0.05797	0.00153	0.42793	0.00903	0.05354	0.00085	529	59	362	6	336	5
19	126.7	22.9	0.18	0.05965	0.00219	0.43807	0.01433	0.05326	0.00089	591	82	369	10	335	5
20	87.6	14.6	0.17	0.05683	0.00222	0.4146	0.01458	0.05291	0.00089	485	88	352	10	332	5
21	158.1	13.4	0.08	0.05436	0.00122	0.45079	0.00846	0.06013	0.00096	386	19	378	6	376	6
22	166.3	26.8	0.16	0.0539	0.00156	0.40149	0.01044	0.05401	0.0009	367	30	343	8	339	6
23	242.2	33.4	0.14	0.05443	0.00119	0.4029	0.00734	0.05368	0.00086	389	18	344	5	337	5
24	472.3	24.0	0.05	0.05396	0.00111	0.39979	0.00669	0.05373	0.00085	369	17	341	5	337	5
25	111.8	16.0	0.14	0.05435	0.00131	0.40392	0.00831	0.05389	0.00087	386	21	344	6	338	5
26	126.6	18.4	0.14	0.06299	0.00181	0.46138	0.011	0.05312	0.00085	708	62	385	8	334	5
27	156.2	23.4	0.15	0.05351	0.00141	0.39626	0.00834	0.05371	0.00085	350	61	339	6	337	5
28	113.4	17.9	0.16	0.05418	0.00159	0.40144	0.00985	0.05374	0.00086	378	67	343	7	337	5
29	69.6	11.9	0.17	0.06412	0.00181	0.47144	0.01095	0.05332	0.00085	746	61	392	8	335	5
30	161.2	27.9	0.17	0.05937	0.00165	0.44812	0.01018	0.05474	0.00087	581	62	376	7	344	5
ZH15-1, Syenogranite: weighted mean age: 332.3±1.6 Ma, n=40, (MSWD = 0.029)															
1	257.0	49.5	0.19	0.05322	0.00117	0.3889	0.00706	0.053	0.00084	338	18	334	5	333	5
2	211.1	31.5	0.15	0.05303	0.0012	0.38415	0.00728	0.05254	0.00083	330	19	330	5	330	5
3	182.4	26.5	0.15	0.05476	0.00206	0.39904	0.01389	0.05285	0.00092	402	47	341	10	332	6
4	269.1	44.0	0.16	0.05309	0.0017	0.386	0.01121	0.05274	0.00088	333	37	331	8	331	5
5	157.3	21.3	0.14	0.05392	0.00245	0.39467	0.01689	0.05309	0.00098	368	63	338	12	333	6
6	195.5	16.9	0.09	0.05314	0.00119	0.38793	0.00719	0.05295	0.00084	335	19	333	5	333	5
7	392.5	60.9	0.16	0.05321	0.00111	0.38852	0.00654	0.05295	0.00083	338	17	333	5	333	5
8	199.3	27.8	0.14	0.05416	0.00152	0.39495	0.00919	0.05288	0.00083	378	65	338	7	332	5
9	156.8	20.2	0.13	0.05337	0.0012	0.38948	0.0073	0.05292	0.00084	345	19	334	5	332	5
10	185.5	18.6	0.10	0.05239	0.00116	0.3823	0.00701	0.05292	0.00083	302	19	329	5	332	5
11	430.6	37.4	0.09	0.05289	0.00153	0.38609	0.00996	0.05294	0.00087	324	31	332	7	333	5
12	156.0	16.3	0.10	0.05394	0.00234	0.39351	0.01602	0.05291	0.00096	369	59	337	12	332	6
13	199.5	21.7	0.11	0.05935	0.0018	0.43211	0.0111	0.05281	0.00084	580	67	365	8	332	5
14	358.0	59.3	0.17	0.05316	0.00121	0.38793	0.0074	0.05292	0.00084	336	20	333	5	332	5
15	156.1	16.3	0.10	0.0531	0.00119	0.3873	0.00722	0.05289	0.00083	333	19	332	5	332	5
16	328.8	24.9	0.08	0.0539	0.00183	0.43459	0.01349	0.05847	0.00099	367	40	366	10	366	6
17	339.7	33.7	0.10	0.05326	0.00133	0.38832	0.0076	0.05288	0.00082	340	58	333	6	332	5
18	131.3	18.0	0.14	0.05332	0.00123	0.38911	0.00751	0.05292	0.00083	342	20	334	5	332	5
19	211.8	29.4	0.14	0.05392	0.00121	0.39304	0.00727	0.05286	0.00083	368	19	337	5	332	5
20	134.6	18.9	0.14	0.05357	0.00155	0.39084	0.0101	0.0529	0.00086	353	31	335	7	332	5
21	603.8	102.7	0.17	0.0541	0.00152	0.44061	0.01092	0.05906	0.00096	375	29	371	8	370	6
22	565.9	72.1	0.13	0.05403	0.00137	0.43784	0.00955	0.05876	0.00094	372	23	369	7	368	6
23	168.4	21.1	0.13	0.05402	0.00131	0.441	0.00905	0.05919	0.00094	372	21	371	6	371	6
24	439.0	31.9	0.07	0.05312	0.00111	0.38476	0.00644	0.05253	0.00082	334	17	331	5	330	5
25	251.6	41.5	0.16	0.05359	0.00121	0.40274	0.00755	0.05449	0.00086	354	19	344	5	342	5
26	176.7	22.7	0.13	0.0541	0.0014	0.40863	0.00919	0.05477	0.00088	375	25	348	7	344	5
27	130.1	15.1	0.12	0.05355	0.00131	0.39035	0.00813	0.05286	0.00084	352	22	335	6	332	5
28	201.3	20.6	0.10	0.05319	0.00118	0.38855	0.0071	0.05297	0.00083	337	19	333	5	333	5
29	243.9	37.2	0.15	0.05314	0.00117	0.38725	0.00699	0.05285	0.00083	335	18	332	5	332	5
30	155.6	17.6	0.11	0.05339	0.00184	0.38911	0.01229	0.05285	0.00089	345	42	334	9	332	5
31	220.7	3.5	0.02	0.0535	0.00121	0.39061	0.00728	0.05294	0.00083	350	19	335	5	333	5
32	248.2	25.0	0.10	0.05338	0.00117	0.39015	0.00701	0.05299	0.00083	345	18	334	5	333	5
33	146.4	16.2	0.11	0.05383	0.00127	0.39265	0.00781	0.05289	0.00083	364	21	336	6	332	5
34	197.8	26.9	0.14	0.05319	0.00117	0.38835	0.00698	0.05294	0.00083	337	18	333	5	333	5
35	325.7	47.8	0.15	0.05312	0.00116	0.38766	0.00687	0.05291	0.00082	334	18	333	5	332	5
36	128.1	17.4	0.14	0.05314	0.00128	0.3882	0.00793	0.05297	0.00083	335	22	333	6	333	5
37	168.3	22.3	0.13	0.05366	0.00139	0.41316	0.00922	0.05583	0.00089	357	24	351	7	350	5
38	242.1	33.0	0.14	0.05391	0.00144	0.39318	0.00912	0.05288	0.00085	367	26	337	7	332	5

Continud Table 1

Spots	^{238}U (ppm)	^{232}Th (ppm)	^{232}Th/^{238}U	Ratio						Age					
				^{207}Pb*/^{206}Pb*		^{207}Pb*/^{235}U		^{206}Pb*/^{238}U		^{207}Pb*/^{206}Pb*		^{207}Pb*/^{235}U		^{206}Pb*/^{238}U	
				ratio	±%	ratio	±%	ratio	±%	age	1σ	age	1σ	age	1σ
39	222.6	30.4	0.14	0.05333	0.00126	0.3976	0.0079	0.05405	0.00085	343	21	340	6	339	5
40	163.2	18.9	0.12	0.0532	0.0016	0.38886	0.01045	0.053	0.00086	337	33	334	8	333	5
41	168.7	15.0	0.09	0.05344	0.00129	0.38954	0.00793	0.05285	0.00083	348	21	334	6	332	5
42	277.0	38.6	0.14	0.05308	0.00115	0.38757	0.00678	0.05295	0.00082	332	18	333	5	333	5
43	153.9	13.8	0.09	0.0534	0.00126	0.39028	0.0077	0.05299	0.00083	346	20	335	6	333	5
44	169.6	27.9	0.16	0.05344	0.00147	0.38971	0.00944	0.05287	0.00085	348	28	334	7	332	5
45	256.3	41.4	0.16	0.05373	0.00225	0.41948	0.01646	0.0566	0.001	360	57	356	12	355	6
46	161.1	18.0	0.11	0.05327	0.00187	0.38828	0.01248	0.05285	0.00089	340	43	333	9	332	5
47	257.9	48.3	0.19	0.05329	0.00129	0.38878	0.00794	0.05289	0.00083	341	22	333	6	332	5
48	307.4	48.4	0.16	0.05324	0.00117	0.38904	0.00693	0.05298	0.00082	339	18	334	5	333	5
49	161.8	21.0	0.13	0.05372	0.0013	0.39274	0.00802	0.053	0.00083	359	21	336	6	333	5
50	203.0	19.4	0.10	0.05394	0.00239	0.39335	0.0164	0.05287	0.00095	369	62	337	12	332	6
51	187.0	20.5	0.11	0.05357	0.0013	0.38748	0.00793	0.05244	0.00082	353	22	333	6	329	5
52	256.8	45.0	0.18	0.05366	0.00122	0.39202	0.00736	0.05297	0.00083	357	19	336	5	333	5
53	190.3	32.1	0.17	0.05387	0.00127	0.39334	0.00772	0.05294	0.00083	366	20	337	6	333	5
54	248.0	52.9	0.21	0.05384	0.00124	0.3926	0.00747	0.05287	0.00082	364	19	336	5	332	5
55	302.1	41.0	0.14	0.05403	0.00119	0.40534	0.00729	0.05439	0.00084	372	18	346	5	341	5
56	210.9	29.5	0.14	0.05342	0.00217	0.39151	0.01481	0.05313	0.00093	347	54	335	11	334	6
57	163.6	21.7	0.13	0.05373	0.00138	0.40456	0.00889	0.05459	0.00086	360	24	345	6	343	5
58	270.8	39.2	0.14	0.05314	0.0012	0.3874	0.00718	0.05285	0.00082	335	19	332	5	332	5
59	118.2	13.8	0.12	0.05308	0.0026	0.38912	0.01801	0.05315	0.00098	332	71	334	13	334	6
60	318.6	51.1	0.16	0.05327	0.00153	0.38835	0.00988	0.05286	0.00085	340	30	333	7	332	5
RG32-1-1, Syenogranite: weighted mean age: 327.1±2.0 Ma, *n*=23, (MSWD = 0.018)															
1	103.4	10.5	0.10	0.05418	0.0012	0.41506	0.00744	0.05549	0.00084	379	18	353	5	348	5
2	145.0	17.9	0.12	0.05325	0.00112	0.38298	0.00633	0.05209	0.00079	339	17	329	5	327	5
3	68.4	11.5	0.17	0.05365	0.00184	0.38454	0.01198	0.05193	0.00085	356	41	330	9	326	5
4	252.7	53.2	0.21	0.05316	0.00107	0.38208	0.00594	0.05207	0.00079	336	16	329	4	327	5
5	121.8	16.6	0.14	0.05315	0.00111	0.38265	0.00626	0.05216	0.00079	335	17	329	5	328	5
6	309.1	28.8	0.09	0.05327	0.00107	0.38357	0.0059	0.05217	0.00079	340	16	330	4	328	5
7	148.2	21.3	0.14	0.05467	0.00112	0.39262	0.00627	0.05205	0.00079	399	16	336	5	327	5
8	81.5	18.0	0.22	0.05327	0.00153	0.38317	0.0097	0.05213	0.00083	340	30	329	7	328	5
9	88.4	18.0	0.20	0.05392	0.00114	0.38785	0.00652	0.05213	0.0008	368	17	333	5	328	5
10	155.8	17.7	0.11	0.05442	0.00113	0.3908	0.00633	0.05206	0.00079	388	16	335	5	327	5
11	71.4	8.4	0.12	0.05398	0.00134	0.43108	0.00903	0.0579	0.0009	370	22	364	6	363	5
12	125.9	17.8	0.14	0.05353	0.0011	0.40856	0.00659	0.05534	0.00085	351	16	348	5	347	5
13	77.6	8.3	0.11	0.05434	0.00173	0.39092	0.0112	0.05216	0.00085	385	36	335	8	328	5
14	48.9	11.0	0.23	0.05348	0.00123	0.38283	0.00728	0.05191	0.0008	349	20	329	5	326	5
15	73.5	10.6	0.14	0.05362	0.00146	0.41025	0.00973	0.05548	0.00088	355	27	349	7	348	5
16	55.3	7.2	0.13	0.05596	0.00167	0.40118	0.01022	0.05199	0.00081	451	68	343	7	327	5
17	122.4	17.5	0.14	0.05383	0.00111	0.38749	0.00629	0.0522	0.0008	364	16	333	5	328	5
18	96.6	15.2	0.16	0.05385	0.00114	0.38603	0.00653	0.05198	0.0008	365	17	331	5	327	5
19	132.9	21.0	0.16	0.05901	0.00156	0.42303	0.00904	0.05199	0.0008	567	59	358	6	327	5
20	216.4	27.4	0.13	0.0541	0.00112	0.38805	0.00629	0.05202	0.0008	375	16	333	5	327	5
21	71.3	14.3	0.20	0.05308	0.00158	0.38106	0.01012	0.05206	0.00085	332	32	328	7	327	5
22	114.9	27.6	0.24	0.0543	0.00121	0.38846	0.00704	0.05189	0.00081	384	18	333	5	326	5
23	99.8	20.5	0.21	0.05352	0.00124	0.40864	0.00789	0.05538	0.00087	351	20	348	6	347	5
24	175.6	30.0	0.17	0.05403	0.00121	0.38729	0.0071	0.052	0.00081	372	19	332	5	327	5
25	87.2	13.8	0.16	0.05317	0.00136	0.38113	0.00838	0.052	0.00083	336	24	328	6	327	5
26	82.6	16.4	0.20	0.05625	0.0017	0.40323	0.01043	0.05199	0.00082	462	69	344	8	327	5
27	291.6	40.8	0.14	0.05316	0.00111	0.38063	0.00634	0.05194	0.00081	336	17	328	5	326	5
28	71.3	13.0	0.18	0.05339	0.00134	0.38246	0.00824	0.05197	0.00083	345	23	329	6	327	5
RG40-5, Syenogranite: weighted mean age: 330.8±1.9 Ma, *n*=26, (MSWD = 0.045)															
1	264.6	14.8	0.06	0.05355	0.0011	0.39028	0.00631	0.05285	0.00082	352	16	335	5	332	5
2	78.6	11.4	0.14	0.05346	0.00249	0.39079	0.01718	0.05301	0.00097	348	66	335	13	333	6
3	125.7	10.6	0.08	0.05322	0.00111	0.38902	0.00644	0.053	0.00082	338	17	334	5	333	5
4	54.7	11.4	0.21	0.06107	0.00179	0.44357	0.01101	0.05268	0.00083	642	65	373	8	331	5
5	52.3	7.6	0.14	0.05414	0.00153	0.42664	0.01062	0.05715	0.00092	377	29	361	8	358	6
6	428.7	28.7	0.07	0.05615	0.00163	0.40842	0.00998	0.05276	0.00083	458	66	348	7	331	5
7	81.8	16.9	0.21	0.05315	0.00115	0.3867	0.0068	0.05276	0.00082	335	18	332	5	331	5
8	84.5	17.1	0.20	0.05381	0.00115	0.39047	0.00674	0.05262	0.00082	363	17	335	5	331	5
9	244.1	13.7	0.06	0.05399	0.00143	0.41926	0.00965	0.05631	0.0009	371	26	356	7	353	5
10	250.4	65.6	0.26	0.05307	0.00109	0.38323	0.00624	0.05237	0.00081	332	17	329	5	329	5
11	101.6	14.2	0.14	0.05526	0.00149	0.40254	0.00892	0.05283	0.00082	423	62	343	6	332	5
12	142.4	16.9	0.12	0.0531	0.00134	0.38549	0.0083	0.05264	0.00084	333	23	331	6	331	5
13	214.5	13.5	0.06	0.05708	0.00129	0.4158	0.00775	0.05282	0.00083	495	18	353	6	332	5
14	82.3	22.0	0.27	0.12314	0.00271	6.15053	0.11043	0.36221	0.0058	2002	14	1997	16	1993	27
15	207.2	50.8	0.25	0.0535	0.00117	0.38786	0.00687	0.05257	0.00082	350	18	333	5	330	5
16	193.2	21.4	0.11	0.05399	0.00111	0.39209	0.0064	0.05267	0.00082	371	17	336	5	331	5
17	229.4	45.8	0.20	0.05464	0.00112	0.39699	0.00643	0.05269	0.00082	398	16	339	5	331	5
18	346.5	26.4	0.08	0.05478	0.00111	0.39759	0.00634	0.05263	0.00082	403	16	340	5	331	5

Continued Table 1

Spots	^{238}U (ppm)	^{232}Th (ppm)	$^{232}Th/^{238}U$	Ratio						Age					
				$^{207}Pb^*/^{206}Pb^*$		$^{207}Pb^*/^{235}U$		$^{206}Pb^*/^{238}U$		$^{207}Pb^*/^{206}Pb^*$		$^{207}Pb^*/^{235}U$		$^{206}Pb^*/^{238}U$	
				ratio	±%	ratio	±%	ratio	±%	age	1σ	age	1σ	age	1σ
19	74.2	9.8	0.13	0.05423	0.00124	0.39399	0.00745	0.05269	0.00083	381	19	337	5	331	5
20	81.7	13.7	0.17	0.06091	0.00177	0.43936	0.01076	0.05232	0.00082	636	64	370	8	329	5
21	122.7	24.4	0.20	0.05405	0.00114	0.39179	0.00659	0.05256	0.00082	373	17	336	5	330	5
22	180.5	64.5	0.36	0.04942	0.00115	0.35815	0.00697	0.05255	0.00083	168	21	311	5	330	5
23	281.6	45.0	0.16	0.05352	0.00152	0.38814	0.00972	0.05259	0.00086	351	29	333	7	330	5
24	286.5	24.9	0.09	0.05308	0.00112	0.38486	0.0065	0.05258	0.00082	332	17	331	5	330	5
25	187.2	16.0	0.09	0.05397	0.00114	0.39218	0.00661	0.05269	0.00082	370	17	336	5	331	5
26	99.1	17.2	0.17	0.05608	0.00184	0.40882	0.0122	0.05286	0.00089	456	37	348	9	332	5
27	55.9	11.5	0.21	0.05398	0.00187	0.39008	0.01235	0.0524	0.00089	370	41	334	9	329	5
28	162.1	14.5	0.09	0.05502	0.00126	0.39886	0.00758	0.05257	0.00083	413	19	341	6	330	5
29	117.9	22.4	0.19	0.0547	0.00123	0.39679	0.00735	0.0526	0.00083	400	19	339	5	330	5
30	74.8	17.8	0.24	0.05765	0.00168	0.41889	0.0103	0.0527	0.00083	516	66	355	7	331	5
RG42-2, Syenogranite: weighted mean age: 346.1±2.2 Ma, *n*=22, (MSWD = 0.103)															
1	55.8	11.8	0.21	0.05458	0.00125	0.41653	0.00785	0.05534	0.00087	395	19	354	6	347	5
2	67.4	10.0	0.15	0.05907	0.00368	0.44332	0.02618	0.05443	0.00108	570	140	373	18	342	7
3	157.1	23.1	0.15	0.05418	0.00114	0.41291	0.00694	0.05527	0.00086	379	17	351	5	347	5
4	151.1	30.1	0.20	0.05407	0.00125	0.41195	0.00791	0.05525	0.00087	374	20	350	6	347	5
5	100.8	23.2	0.23	0.05424	0.00142	0.4125	0.00938	0.05516	0.00088	381	25	351	7	346	5
6	211.1	11.5	0.05	0.11283	0.00228	5.14021	0.08083	0.3304	0.00513	1845	13	1843	13	1840	25
7	17.6	0.5	0.03	0.11856	0.00269	4.99303	0.08309	0.30544	0.00469	1935	41	1818	14	1718	23
8	190.7	40.2	0.21	0.05651	0.00141	0.42845	0.00912	0.05498	0.00087	472	22	362	6	345	5
9	102.1	13.1	0.13	0.05346	0.00113	0.40761	0.00693	0.0553	0.00086	348	17	347	5	347	5
10	173.5	34.0	0.20	0.0548	0.00113	0.41711	0.00684	0.0552	0.00086	404	16	354	5	346	5
11	79.4	13.2	0.17	0.05343	0.00165	0.40661	0.01129	0.05519	0.00091	347	34	346	8	346	6
12	62.9	8.7	0.14	0.05456	0.00239	0.41679	0.01712	0.0554	0.001	394	60	354	12	348	6
13	263.8	48.3	0.18	0.05391	0.00119	0.41009	0.00739	0.05517	0.00086	367	18	349	5	346	5
14	55.0	10.9	0.20	0.05709	0.00312	0.43258	0.02218	0.05496	0.00103	495	124	365	16	345	6
15	110.0	7.4	0.07	0.07034	0.00191	0.52742	0.01169	0.05438	0.00085	938	57	430	8	341	5
16	98.3	12.4	0.13	0.05348	0.00171	0.4072	0.01124	0.05523	0.00089	349	74	347	8	347	5
17	76.4	6.7	0.09	0.05405	0.00137	0.41144	0.00826	0.05521	0.00085	373	58	350	6	346	5
18	82.0	11.3	0.14	0.05468	0.00118	0.45242	0.00788	0.06	0.00094	399	17	379	6	376	6
19	56.7	12.3	0.22	0.05409	0.00145	0.41308	0.00968	0.05539	0.00089	375	26	351	7	348	5
20	260.0	48.1	0.19	0.06923	0.00214	0.52485	0.01385	0.05498	0.00088	906	65	428	9	345	5
21	78.8	12.3	0.16	0.05403	0.00116	0.41227	0.00721	0.05534	0.00087	372	18	351	5	347	5
22	266.3	191.7	0.72	0.11652	0.00236	5.47928	0.08718	0.34101	0.00533	1904	13	1897	14	1892	26
23	198.8	32.6	0.16	0.05407	0.00154	0.41146	0.01041	0.05519	0.0009	374	29	350	7	346	5
24	111.8	17.9	0.16	0.0536	0.0018	0.40676	0.01248	0.05504	0.00093	354	40	347	9	345	6
25	160.2	25.1	0.16	0.05479	0.00114	0.41851	0.00695	0.0554	0.00087	404	17	355	5	348	5
26	89.0	17.7	0.20	0.05472	0.0012	0.41742	0.00748	0.05532	0.00087	401	18	354	5	347	5
RG55-3, Syenogranite: weighted mean age: 331.4±2.1 Ma, *n*=26, (MSWD = 0.031)															
1	106.8	11.6	0.11	0.05343	0.00135	0.38768	0.00847	0.05262	0.00084	347	24	333	6	331	5
2	144.1	24.0	0.17	0.05345	0.00396	0.39285	0.02808	0.0533	0.00122	348	120	336	20	335	7
3	176.2	28.0	0.16	0.05423	0.00184	0.39294	0.01216	0.05254	0.00089	381	40	337	9	330	5
4	147.8	20.9	0.14	0.05807	0.00423	0.4216	0.02924	0.05265	0.00117	532	165	357	21	331	7
5	401.9	31.8	0.08	0.05907	0.00215	0.42864	0.01437	0.05262	0.00091	570	43	362	10	331	6
6	63.7	14.8	0.23	0.05904	0.00174	0.42795	0.0113	0.05257	0.00087	569	30	362	8	330	5
7	135.1	14.5	0.11	0.05462	0.00148	0.39772	0.00945	0.05281	0.00086	397	26	340	7	332	5
8	123.2	26.9	0.22	0.05316	0.00181	0.38467	0.01202	0.05248	0.00089	336	41	330	9	330	5
9	200.5	47.8	0.24	0.05342	0.00124	0.38927	0.0076	0.05284	0.00084	347	20	334	6	332	5
10	89.4	12.8	0.14	0.05449	0.00179	0.39681	0.01184	0.05281	0.00089	391	38	339	9	332	5
11	191.2	53.3	0.28	0.05482	0.00126	0.3977	0.00765	0.05261	0.00084	405	19	340	6	331	5
12	162.3	23.0	0.14	0.05446	0.00244	0.39636	0.01673	0.05278	0.00097	390	62	339	12	332	6
13	86.9	18.2	0.21	0.0543	0.00144	0.3957	0.00915	0.05284	0.00086	384	25	339	7	332	5
14	105.5	17.8	0.17	0.05351	0.00173	0.38848	0.0114	0.05265	0.00088	350	37	333	8	331	5
15	210.1	17.6	0.08	0.05403	0.0025	0.39282	0.01715	0.05272	0.00098	372	65	336	13	331	6
16	264.7	44.3	0.17	0.05393	0.00313	0.39209	0.02176	0.05273	0.00107	368	88	336	16	331	7
17	292.2	16.7	0.06	0.05314	0.00126	0.38581	0.00775	0.05265	0.00084	335	21	331	6	331	5
18	148.2	26.7	0.18	0.05318	0.00191	0.38641	0.01281	0.05269	0.00091	336	44	332	9	331	6
19	341.4	87.6	0.26	0.05305	0.0012	0.3848	0.00725	0.05261	0.00084	331	19	331	5	331	5
20	227.1	56.0	0.25	0.05335	0.002	0.3876	0.01349	0.05269	0.00092	344	48	333	10	331	6
21	160.3	9.1	0.06	0.05378	0.00276	0.39185	0.01872	0.05284	0.00098	362	119	336	14	332	6
22	172.4	24.3	0.14	0.0545	0.00257	0.3973	0.01774	0.05286	0.00099	392	67	340	13	332	6
23	307.1	90.2	0.29	0.05419	0.003	0.39424	0.0208	0.05276	0.00105	379	83	337	15	331	6
24	544.6	38.4	0.07	0.0582	0.00376	0.4247	0.02628	0.05292	0.00115	537	97	359	19	332	7
25	110.4	18.9	0.17	0.05325	0.00134	0.38892	0.0085	0.05297	0.00086	339	23	334	6	333	5
26	159.7	33.7	0.21	0.05352	0.00126	0.39008	0.00783	0.05286	0.00085	351	21	334	6	332	5

Table 2 Zircon Hf isotopic compositions of Dabashan pluton in the southern Langshan

Spots		$^{176}Yb/^{177}Hf$	±2σ	$^{176}Lu/^{177}Hf$	±2σ	$^{176}Hf/^{177}Hf$	±2σ	$^{176}Hf/^{177}Hf_i$	$\varepsilon_{Hf}(0)$	$\varepsilon_{Hf}(t)$	T_{DM1} (Ma)	T_{DM2} (Ma)	$f_{Lu/Hf}$
ZH15-1-01	333	0.054865	0.000805	0.001794	0.000026	0.282073	0.000018	0.282062	−24.72	−17.81	1697	2457	−0.95
ZH15-1-02	330	0.044699	0.000578	0.001477	0.000016	0.282122	0.000017	0.282113	−22.98	−16.07	1613	2346	−0.96
ZH15-1-04	331	0.055500	0.000347	0.001796	0.000011	0.282127	0.000018	0.282116	−22.81	−15.95	1621	2340	−0.95
ZH15-1-05	333	0.047112	0.000727	0.001659	0.000025	0.282106	0.000019	0.282096	−23.54	−16.61	1644	2382	−0.95
ZH15-1-06	333	0.046009	0.000554	0.001517	0.000019	0.282077	0.000017	0.282067	−24.59	−17.62	1679	2446	−0.95
ZH15-1-07	333	0.062951	0.001138	0.002034	0.000039	0.282051	0.000019	0.282038	−25.50	−18.64	1739	2509	−0.94
ZH15-1-08	332	0.039498	0.001218	0.001277	0.000036	0.282064	0.000017	0.282056	−25.04	−18.04	1686	2471	−0.96
ZH15-1-09	332	0.049774	0.000532	0.001612	0.000018	0.282114	0.000018	0.282104	−23.25	−16.33	1630	2364	−0.95
ZH15-1-14	332	0.058056	0.000396	0.001872	0.000012	0.282079	0.000018	0.282067	−24.51	−17.64	1692	2446	−0.94
ZH15-1-15	332	0.046146	0.000794	0.001515	0.000022	0.282082	0.000017	0.282073	−24.40	−17.45	1672	2434	−0.95
ZH15-1-16	332	0.071866	0.000371	0.002209	0.000009	0.282100	0.000016	0.282087	−23.76	−16.96	1677	2403	−0.93
ZH15-1-17	332	0.054644	0.000348	0.001795	0.000016	0.282072	0.000020	0.282061	−24.74	−17.86	1698	2459	−0.95
ZH15-1-18	332	0.058530	0.000396	0.001831	0.000011	0.282141	0.000016	0.282130	−22.30	−15.42	1601	2307	−0.94
ZH15-1-21	368	0.067165	0.000814	0.002117	0.000022	0.282120	0.000019	0.282106	−23.04	−15.49	1644	2338	−0.94
ZH15-1-23	330	0.044996	0.000959	0.001430	0.000024	0.282102	0.000015	0.282093	−23.70	−16.77	1640	2391	−0.96
ZH15-1-26	332	0.044268	0.001270	0.001441	0.000041	0.282117	0.000018	0.282108	−23.15	−16.19	1619	2355	−0.96
ZH15-1-27	333	0.051436	0.000478	0.001641	0.000013	0.282077	0.000016	0.282067	−24.56	−17.62	1684	2446	−0.95
ZH15-1-28	332	0.056139	0.000698	0.001799	0.000019	0.282111	0.000016	0.282100	−23.39	−16.50	1644	2375	−0.95
ZH15-1-29	332	0.054367	0.000707	0.001686	0.000016	0.282077	0.000015	0.282066	−24.58	−17.67	1687	2448	−0.95
ZH15-1-30	333	0.021173	0.000236	0.000776	0.000007	0.282072	0.000011	0.282067	−24.77	−17.64	1653	2447	−0.98
ZH15-1-32	332	0.045510	0.000462	0.001459	0.000017	0.282065	0.000017	0.282056	−25.01	−18.05	1693	2472	−0.96
RG32-1-01	348	0.048035	0.000308	0.001341	0.000010	0.282062	0.000022	0.282054	−25.10	−17.77	1691	2466	−0.96
RG32-1-02	327	0.044318	0.000638	0.001274	0.000023	0.282052	0.000021	0.282045	−25.45	−18.55	1702	2500	−0.96
RG32-1-03	326	0.059811	0.000644	0.001618	0.000011	0.282134	0.000019	0.282124	−22.57	−15.77	1603	2325	−0.95
RG32-1-05	328	0.029177	0.000417	0.000848	0.000015	0.282058	0.000019	0.282053	−25.24	−18.24	1675	2481	−0.97
RG32-1-06	328	0.054270	0.000290	0.001575	0.000011	0.282080	0.000018	0.282070	−24.47	−17.62	1677	2442	−0.95
RG32-1-09	328	0.058340	0.000980	0.001640	0.000023	0.282088	0.000020	0.282078	−24.19	−17.35	1669	2425	−0.95
RG32-1-10	327	0.055534	0.001807	0.001500	0.000043	0.282101	0.000016	0.282092	−23.72	−16.87	1644	2394	−0.95
RG32-1-11	363	0.046668	0.001545	0.001357	0.000044	0.282087	0.000019	0.282078	−24.22	−16.58	1657	2403	−0.96
RG32-1-12	347	0.039967	0.000812	0.001184	0.000014	0.282070	0.000020	0.282063	−24.82	−17.48	1673	2447	−0.96
RG32-1-16	327	0.038914	0.000604	0.001142	0.000020	0.282057	0.000020	0.282050	−25.29	−18.37	1690	2488	−0.97
RG32-1-18	327	0.031981	0.000737	0.001017	0.000030	0.282066	0.000021	0.282060	−24.96	−18.01	1671	2466	−0.97
RG32-1-19	327	0.081087	0.001292	0.002239	0.000030	0.282085	0.000015	0.282071	−24.30	−17.61	1700	2440	−0.93
RG32-1-20	327	0.048688	0.000258	0.001377	0.000007	0.282059	0.000018	0.282050	−25.23	−18.36	1698	2487	−0.96
RG32-1-21	327	0.056445	0.000242	0.001609	0.000016	0.282091	0.000016	0.282081	−24.09	−17.27	1663	2419	−0.95
RG32-1-22	326	0.065988	0.000685	0.001852	0.000020	0.282027	0.000016	0.282016	−26.33	−19.58	1764	2563	−0.94
RG32-1-23	347	0.053712	0.000471	0.001529	0.000009	0.282096	0.000021	0.282086	−23.92	−16.66	1653	2396	−0.95
RG32-1-24	327	0.063389	0.000701	0.001772	0.000012	0.282157	0.000018	0.282147	−21.73	−14.95	1576	2274	−0.95
RG32-1-25	327	0.069620	0.000894	0.002138	0.000042	0.282063	0.000021	0.282049	−25.09	−18.38	1728	2488	−0.94
RG32-1-26	327	0.059501	0.000426	0.001839	0.000022	0.282013	0.000018	0.282001	−26.85	−20.08	1785	2595	−0.94
RG32-1-27	326	0.052705	0.000329	0.001555	0.000008	0.282072	0.000019	0.282063	−24.74	−17.93	1687	2459	−0.95
RG32-1-28	327	0.049461	0.000812	0.001495	0.000036	0.282117	0.000019	0.282108	−23.15	−16.31	1621	2359	−0.95
RG40-5-01	332	0.043167	0.000378	0.001357	0.000010	0.282122	0.000015	0.282113	−23.00	−16.02	1609	2345	−0.96
RG40-5-02	333	0.031413	0.000443	0.001058	0.000009	0.282055	0.000025	0.282049	−25.35	−18.28	1689	2487	−0.97
RG40-5-03	333	0.038919	0.000764	0.001248	0.000028	0.282077	0.000018	0.282069	−24.58	−17.55	1667	2442	−0.96
RG40-5-07	331	0.053171	0.000674	0.001600	0.000020	0.282037	0.000019	0.282027	−25.98	−19.08	1739	2535	−0.95

Continued Table 2

Spots		$^{176}Yb/^{177}Hf$	±2σ	$^{176}Lu/^{177}Hf$	±2σ	$^{176}Hf/^{177}Hf$	±2σ	$^{176}Hf/^{177}Hf_i$	$\varepsilon_{Hf}(0)$	$\varepsilon_{Hf}(t)$	T_{DM1} (Ma)	T_{DM2} (Ma)	$f_{Lu/Hf}$
RG40-5-08	331	0.054132	0.000584	0.001707	0.000017	0.282075	0.000020	0.282064	−24.65	−17.77	1690	2453	−0.95
RG40-5-10	329	0.055173	0.001440	0.001773	0.000058	0.282101	0.000022	0.282090	−23.73	−16.90	1656	2398	−0.95
RG40-5-15	330	0.063218	0.001041	0.002102	0.000041	0.282058	0.000028	0.282045	−25.26	−18.49	1733	2497	−0.94
RG40-5-16	331	0.037416	0.001226	0.001226	0.000027	0.282041	0.000019	0.282033	−25.85	−18.86	1716	2522	−0.96
RG40-5-18	331	0.056763	0.000661	0.001869	0.000031	0.282125	0.000021	0.282113	−22.89	−16.04	1627	2345	−0.94
RG40-5-19	331	0.025612	0.000238	0.000890	0.000009	0.282062	0.000013	0.282057	−25.10	−18.04	1672	2471	−0.97
RG40-5-21	330	0.055293	0.001004	0.001711	0.000020	0.282114	0.000018	0.282104	−23.26	−16.39	1635	2367	−0.95
RG40-5-23	330	0.053006	0.001610	0.001692	0.000064	0.282086	0.000020	0.282076	−24.25	−17.39	1674	2429	−0.95
RG40-5-25	331	0.048218	0.000926	0.001482	0.000026	0.282117	0.000017	0.282108	−23.15	−16.21	1620	2356	−0.96
RG40-5-27	329	0.043748	0.000696	0.001359	0.000022	0.282081	0.000020	0.282073	−24.44	−17.52	1666	2436	−0.96
RG40-5-28	330	0.053941	0.001046	0.001774	0.000029	0.282184	0.000023	0.282173	−20.80	−13.95	1539	2214	−0.95
RG40-5-29	330	0.043175	0.000913	0.001382	0.000035	0.282109	0.000020	0.282100	−23.45	−16.52	1628	2375	−0.96
RG42-2-03	347	0.043906	0.000642	0.001488	0.000026	0.282067	0.000023	0.282057	−24.93	−17.66	1691	2459	−0.96
RG42-2-04	347	0.076497	0.000940	0.002453	0.000033	0.282093	0.000022	0.282077	−24.02	−16.97	1699	2415	−0.93
RG42-2-05	346	0.044120	0.000740	0.001289	0.000019	0.282080	0.000019	0.282072	−24.47	−17.17	1664	2427	−0.96
RG42-2-08	345	0.077224	0.000798	0.002501	0.000023	0.282138	0.000025	0.282122	−22.41	−15.41	1635	2316	−0.92
RG42-2-09	347	0.049127	0.000662	0.001429	0.000018	0.282060	0.000019	0.282051	−25.17	−17.89	1698	2473	−0.96
RG42-2-01	347	0.055738	0.001322	0.001680	0.000026	0.282085	0.000021	0.282074	−24.29	−17.06	1674	2421	−0.95
RG42-2-10	346	0.066788	0.000913	0.001932	0.000039	0.282098	0.000019	0.282085	−23.85	−16.71	1668	2398	−0.94
RG42-2-11	346	0.046633	0.000542	0.001363	0.000018	0.282066	0.000017	0.282057	−24.98	−17.70	1688	2461	−0.96
RG42-2-12	348	0.042211	0.000292	0.001238	0.000005	0.282064	0.000019	0.282056	−25.04	−17.69	1684	2461	−0.96
RG42-2-14	345	0.037241	0.000367	0.001293	0.000012	0.282105	0.000018	0.282097	−23.59	−16.32	1630	2373	−0.96
RG42-2-16	347	0.062465	0.001135	0.002044	0.000039	0.282140	0.000023	0.282127	−22.35	−15.20	1612	2305	−0.94
RG42-2-17	346	0.046875	0.001144	0.001436	0.000022	0.282126	0.000017	0.282117	−22.85	−15.59	1606	2328	−0.96
RG42-2-23	346	0.035771	0.000844	0.001084	0.000016	0.282089	0.000015	0.282082	−24.16	−16.82	1643	2405	−0.97
RG42-2-24	345	0.045595	0.000636	0.001371	0.000023	0.282086	0.000019	0.282077	−24.26	−17.01	1660	2416	−0.96
RG42-2-25	348	0.048310	0.000725	0.001386	0.000009	0.282094	0.000018	0.282085	−23.98	−16.67	1649	2397	−0.96
RG42-2-26	347	0.063537	0.000274	0.001880	0.000015	0.282152	0.000018	0.282140	−21.92	−14.74	1588	2276	−0.94
RG55-3-01	331	0.040331	0.000283	0.001228	0.000018	0.282065	0.000017	0.282058	−25.00	−18.01	1682	2469	−0.96
RG55-3-02	335	0.049137	0.000918	0.001752	0.000026	0.282120	0.000022	0.282109	−23.05	−16.09	1628	2351	−0.95
RG55-3-04	331	0.063851	0.001048	0.002099	0.000034	0.282006	0.000026	0.281993	−27.08	−20.29	1806	2610	−0.94
RG55-3-07	332	0.041441	0.001047	0.001212	0.000031	0.282070	0.000018	0.282063	−24.81	−17.80	1674	2456	−0.96
RG55-3-08	330	0.055710	0.000673	0.001659	0.000019	0.282057	0.000019	0.282047	−25.29	−18.41	1713	2493	−0.95
RG55-3-10	332	0.060090	0.000628	0.002081	0.000021	0.282121	0.000020	0.282108	−23.01	−16.19	1641	2355	−0.94
RG55-3-12	332	0.070322	0.000684	0.002356	0.000019	0.282134	0.000028	0.282120	−22.55	−15.79	1635	2330	−0.93
RG55-3-13	332	0.046379	0.000628	0.001509	0.000022	0.282032	0.000024	0.282023	−26.17	−19.22	1742	2545	−0.95
RG55-3-14	331	0.077224	0.000942	0.002342	0.000036	0.282075	0.000022	0.282060	−24.67	−17.92	1720	2462	−0.93
RG55-3-15	331	0.049627	0.001386	0.001475	0.000040	0.282057	0.000018	0.282048	−25.27	−18.34	1704	2489	−0.96
RG55-3-17	331	0.036139	0.000634	0.001112	0.000016	0.282050	0.000018	0.282043	−25.53	−18.52	1698	2500	−0.97
RG55-3-18	331	0.064050	0.002757	0.001793	0.000073	0.282070	0.000017	0.282058	−24.84	−17.98	1702	2466	−0.95
RG55-3-21	332	0.035530	0.000357	0.001121	0.000010	0.282104	0.000019	0.282097	−23.63	−16.59	1624	2381	−0.97
RG55-3-22	332	0.045559	0.000470	0.001565	0.000020	0.282083	0.000023	0.282074	−24.35	−17.41	1672	2432	−0.95
RG55-3-24	332	0.077085	0.000367	0.002590	0.000019	0.282101	0.000020	0.282085	−23.72	−17.01	1693	2406	−0.92
RG55-3-26	332	0.033599	0.000263	0.001170	0.000015	0.282084	0.000018	0.282077	−24.32	−17.30	1653	2425	−0.96

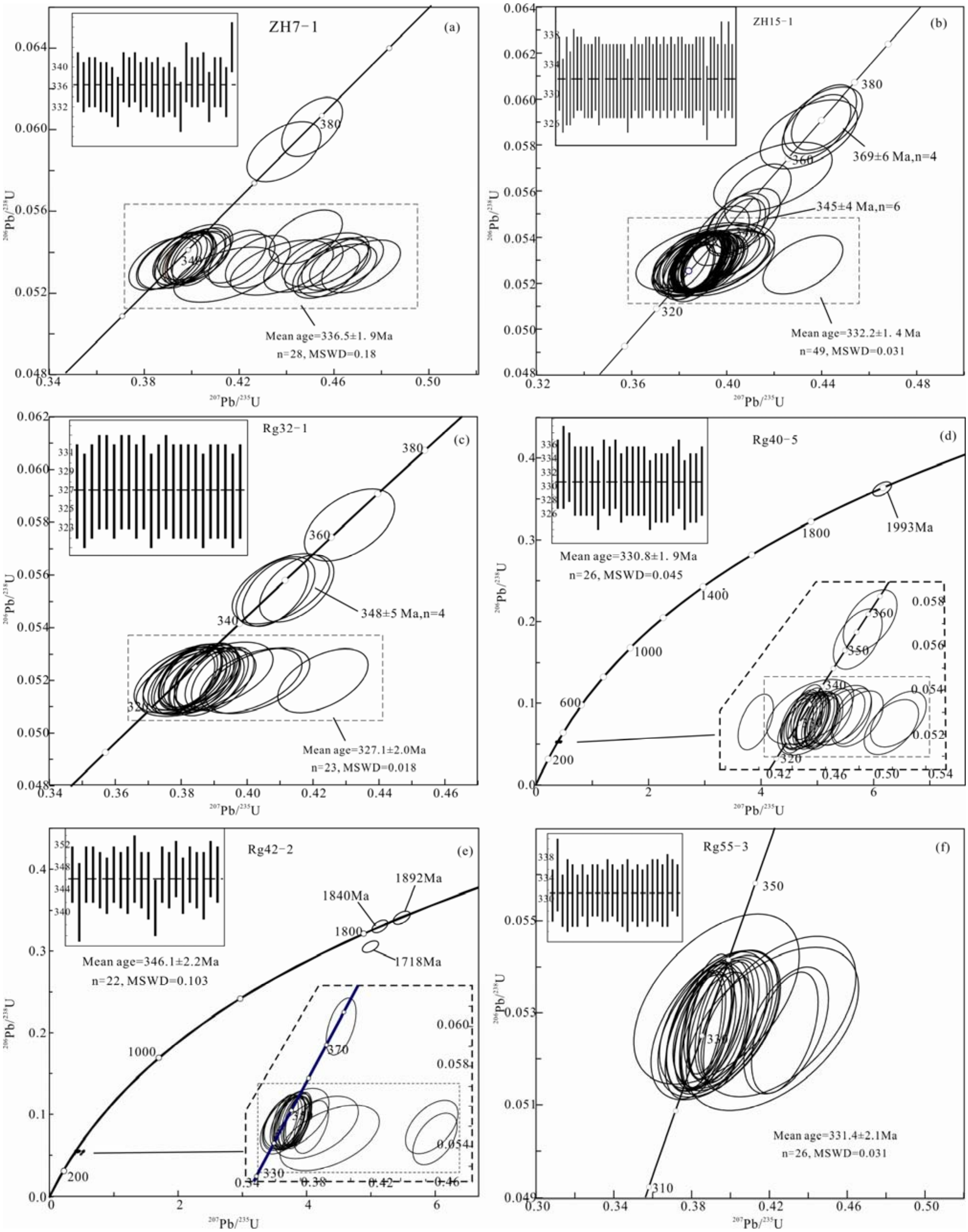

Fig. 5. U–Pb concordia diagrams of zircons from Dabashan pluton in the southern Langshan.

1993 Ma, indicating a more complicated thermal or zircon crystallization history. Twenty-six analyses form a tight cluster in the Concordia diagram, and the weighted mean age (330.8±1.9 Ma, MSWD=0.045, n=26, Fig. 5d) is interpreted

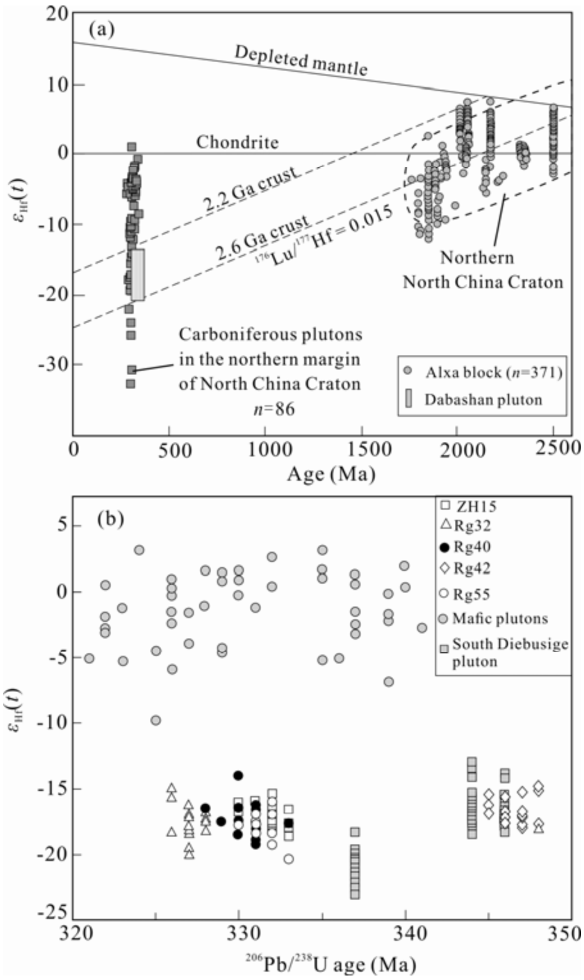

Fig. 6. Zircon $\varepsilon_{Hf}(t)$ vs. $^{206}Pb/^{238}U$ age diagram of Dabashan pluton in the southern Langshan.

Data of Carboniferous plutons in the northern margin of NCC, and areas of northern NCC are from Zhang et al., 2009 and references therein. Data sources of Alxa block are Dan et al., 2012; Zhang et al., 2013b; Gong et al., 2016. Data of mafic plutons are from Liu et al., 2016a; Data of south Diebusige plutons are from Dan et al., 2016.

as the time of magmatic intrusion. 16 zircon grains from sample Rg-40 were analyzed to obtain their Lu–Hf isotopic compositions. The $(^{176}Hf/^{177}Hf)_i$ ratios vary from 0.282027 to 0.282173. All zircon grains exhibit negative $\varepsilon_{Hf}(t)$ values, varying from −13.95 to −19.08 (Fig. 6b), and relatively old T_{DM2} model ages, ranging from 2.21 to 2.54 Ga.

4.1.5 Sample Rg42–2

Twenty-six spots were analyzed for sanple Rg42–2. Four analyses exhibit relatively old $^{206}Pb/^{238}U$ apparent ages, which are 1892 Ma, 1840 Ma, 1718 Ma and 376 Ma. The other twenty-two analyses have close $^{206}Pb/^{238}U$ apparent ages, ranging from 342 Ma to 348 Ma, and give a weighted mean $^{206}Pb/^{238}U$ age of 346.1±2.2 Ma (MSWD=0.103, n=22, Fig. 5e), which may be the crystallization age. 16 zircon grains from sample Rg-42 were analyzed to obtain their Lu–Hf isotopic compositions. The $(^{176}Hf/^{177}Hf)_i$ ratios vary from 0.282051 to 0.282140. All zircon grains exhibit negative $\varepsilon_{Hf}(t)$ values, varying from −14.72 to −17.93 (Fig. 6b), and relatively old T_{DM2} model ages, ranging from 2.28 to 2.47 Ga.

4.1.6 Sample Rg55–3

As to the sample Rg55–3, $^{206}Pb/^{238}U$ apparent ages of 26 analyses range 330 Ma to 335Ma, and the data points form a tight cluster in the Concordia diagram with a weighted mean age of 331.4±2.1 Ma (MSWD=0.031, n=26, Fig. 5f), which is interpreted as the time of magmatic intrusion. 16 zircon grains from sample Rg-55 were analyzed to obtain their Lu–Hf isotopic compositions. The $(^{176}Hf/^{177}Hf)_i$ ratios vary from 0.281993 to 0.282120. All zircon grains exhibit negative $\varepsilon_{Hf}(t)$ values, varying from −15.79 to −20.25 (Fig. 6b), and relatively old T_{DM2} model ages, ranging from 2.33 to 2.61 Ga.

4.2 Whole-rock major and trace element compositions

Major and trace element data of the Dabashan pluton are listed in the Table 3 and presented in figures 7, 8 and 9. All granite samples display some similar geochemical characteristics. All of those samples have relatively high SiO_2 contents (70.58–74.65 wt%), and low contents of MgO, CaO, Fe_2O_3, TiO_2, and P_2O_5. In the R1 versus R2 diagram, all those granites are plotted in the monzogranite and syenogranite fields (Fig. 7a). They are rich in total alkalis (Na_2O+K_2O=7.29–8.41 wt%), exhibit high K_2O/Na_2O ratios (1.13–1.74), and plot in the high-K calc-alkaline field in the SiO_2 versus K_2O diagram (Fig. 7b), revealing an overall potassic character. Their low Rittmann Index values (σ=1.77–2.39) also show calc-alkaline characteristics. They all have high Al_2O_3 contents (13.68–14.77). All the other samples exhibit moderate A/CNK values (1.01–1.14, most < 1.1) and display weak peraluminous characteristics except the Rg40 series, which display strongly peraluminous characteristics with high A/CNK values (1.27–1.42, Fig. 7c). All the samples display ferruginous characteristics (Fig. 7d). In the Harker diagrams (Fig. 8), the content of Al_2O_3, TiO_2, MgO, total Fe_2O_3, and CaO decrease, but there are no obvious correlations between K_2O, Na_2O, Sr and SiO_2 (Fig. 8).

In the Chondrite-normalized rare earth element (REE) diagram (Fig. 9), all the samples display light REE enrichments in relative to heavy REEs [$(La/Yb)_N$ =9.47–78.10], and there are extremely weak differentiations between medium and heavy REEs [$(Gd/Yb)_N$ =1.26–5.33]. They all display moderate negative Eu anomalies (δEu=0.60–0.84) (Fig. 9). In the primitive mantle-normalized multi-element diagram (Fig. 9), samples display enrichments in Rb, Ba, K, Zr and Hf and depletions in Nb, Ta, P, and Ti relative to neighboring elements (Fig. 9). In addition, all the samples exhibit high Ba and Sr, and low Yb and Y concentrations, in particular, samples of the ZH7 series exhibit extremely high Ba (2296–2817 ppm) and Sr (441–520 ppm) with high Sr/Y (59–66) and $(La/Yb)_N$ (70–78), which make them different from all the other samples.

5 Discussion

5.1 Early Carboniferous magmatism in the Langshan region

In previous studies, the Dabashan pluton was

Table 3 Major (wt%) and trace elements (ppm) compositions of Dabashan pluton in the southern Langshan

Sample No.	ZH7-1	ZH7-2	ZH7-3	ZH7-4	ZH7-5	ZH15-1	ZH15-2	ZH15-3	ZH15-4	Rg32-1	Rg32-2	Rg32-3	Rg32-4
SiO_2	71.37	71.38	71.53	70.58	71.55	72.96	72.31	72.09	72.34	74.06	73.73	71.93	72.88
TiO_2	0.32	0.32	0.30	0.32	0.32	0.20	0.25	0.26	0.20	0.15	0.15	0.24	0.16
Al_2O_3	14.18	14.42	14.30	14.37	14.34	14.20	14.27	14.38	14.35	14.06	14.16	14.47	14.22
TFe_2O_3	2.27	2.18	2.13	2.27	2.22	1.50	1.93	1.91	1.60	1.10	1.05	1.66	1.31
FeO	1.40	1.31	1.09	1.41	1.56	0.99	1.38	1.58	0.99	0.48	0.66	0.64	0.60
MnO	0.03	0.02	0.02	0.03	0.03	0.03	0.04	0.04	0.03	0.02	0.02	0.03	0.03
MgO	0.56	0.57	0.57	0.58	0.57	0.40	0.54	0.52	0.40	0.17	0.14	0.31	0.12
CaO	1.95	1.97	1.92	1.90	1.95	1.72	1.83	1.84	1.84	1.22	1.18	1.56	1.29
Na_2O	3.20	3.21	3.35	3.25	3.28	3.56	3.61	3.56	3.79	3.67	3.38	3.41	3.31
K_2O	4.49	4.57	4.52	4.87	4.51	4.73	4.38	4.54	4.28	4.52	4.85	5.00	4.87
P_2O_5	0.08	0.08	0.08	0.08	0.08	0.05	0.07	0.06	0.05	0.04	0.04	0.06	0.04
LOI	1.01	1.27	1.24	1.20	1.14	0.65	0.72	0.74	1.10	0.98	1.28	1.29	1.73
σ	2.08	2.13	2.17	2.39	2.13	2.29	2.18	2.26	2.22	2.16	2.20	2.44	2.24
Li	8.86	6.92	7.73	8.21	8.09	10.20	14.50	12.80	11.10	10.20	12.70	16.50	11.70
Be	0.99	0.88	0.98	1.05	1.57	1.60	1.65	1.43	1.90	2.43	2.06	2.15	2.05
Sc	3.33	2.83	3.24	3.27	3.46	2.97	3.36	3.07	2.97	2.39	2.67	2.84	2.56
V	25	22.7	23.3	24	24.9	17.2	21.9	19.6	17.3	10.8	10.5	17.9	12.1
Cr	5.74	4.43	6.13	4.46	5.29	4.73	6.57	6.37	4.99	6.28	14.3	5.92	9.54
Co	3.37	2.76	2.98	3	3.38	2.01	2.52	2.51	2.17	1.45	1.22	2.32	1.41
Ni	2.17	1.62	2.47	2.04	1.48	0.933	1.39	2.46	1.87	2.64	6.41	2.19	3.12
Ga	16.7	14.7	16	15.6	16.8	16.3	15.7	14.9	17.8	18.4	19.4	18.3	17.9
Rb	67.6	60.5	66.1	70.7	69.5	89.2	86.4	85.3	84.1	119	126	102	113
Sr	496	441	510	459	520	290	303	285	283	201	188	283	166
Y	7.58	6.88	7.72	7.81	8.38	12.4	12.3	13.1	9.78	8.29	11.9	9.24	12.9
Zr	195	156	182	163	173	84.6	137	146	131	91.4	107	136	90.4
Nb	6.9	6.55	7.37	7.32	7.3	12	11.7	12.3	9.79	9.92	14.3	12.6	13.2
Cs	0.33	0.293	0.307	0.356	0.342	0.642	0.688	0.629	0.551	4.91	1.62	2.6	1.04
Ba	2518	2296	2685	2554	2817	1243	1351	1292	1111	823	900	1610	834
La	73.7	65	73.8	73.1	75.7	41.6	53.8	51.5	46.5	23.3	24.6	45.9	21.8
Ce	118	104	117	117	121	65.1	84.4	80.2	74.4	39.2	41.6	74.4	36.7
Pr	11.9	10.3	11.8	11.8	12.3	6.64	8.29	8.11	7.31	4.05	4.36	7.49	3.83
Nd	40.8	36	40.8	40.4	42.5	23.3	28.2	27.8	25.3	14	14.9	24.6	13.4
Sm	5.3	4.77	5.3	5.55	5.69	3.47	3.83	3.91	3.47	2.29	2.47	3.35	2.28
Eu	1.02	0.867	1.02	0.995	1.02	0.755	0.742	0.747	0.769	0.453	0.5	0.692	0.47
Gd	4.17	3.78	4.28	4.17	4.27	2.93	3.32	3.3	2.75	1.78	2.01	2.64	2.05
Tb	0.466	0.41	0.472	0.459	0.475	0.44	0.459	0.426	0.387	0.276	0.355	0.356	0.364
Dy	1.8	1.74	1.88	1.89	2.02	2.34	2.27	2.31	1.79	1.45	1.91	1.6	1.88
Ho	0.287	0.262	0.276	0.284	0.304	0.431	0.413	0.429	0.322	0.252	0.359	0.303	0.393
Er	0.822	0.711	0.758	0.794	0.838	1.26	1.23	1.24	0.944	0.773	1.05	0.933	1.13
Tm	0.103	0.102	0.116	0.101	0.112	0.2	0.189	0.199	0.141	0.139	0.179	0.141	0.195
Yb	0.708	0.6	0.679	0.631	0.714	1.3	1.31	1.31	1.03	0.895	1.24	0.989	1.31
Lu	0.117	0.089	0.114	0.108	0.116	0.174	0.175	0.207	0.165	0.119	0.185	0.133	0.196
Hf	5.32	4.28	5.01	4.61	4.86	2.95	4.29	4.17	4.38	3.32	3.92	4.12	3.13
Ta	0.278	0.232	0.277	0.281	0.298	1.02	0.89	0.978	0.627	0.941	1.3	1.01	1.31
Pb	34.3	30.9	33.3	37.3	35.9	31.2	27.4	26.2	30.9	33.3	40.3	31.8	35.3
Th	5.93	5.28	5.92	5.94	6.17	6.4	7.6	7.46	5.89	4.11	4.33	6.09	3.74
U	0.378	0.331	0.38	0.369	0.4	1.01	1.23	1.19	0.973	0.869	0.683	0.876	0.641
$(La/Sm)_N$	8.75	8.57	8.76	8.29	8.37	7.54	8.84	8.29	8.43	6.40	6.26	8.62	6.01
$(La/Yb)_N$	70.18	73.04	73.28	78.10	71.48	21.57	27.69	26.50	30.44	17.55	13.38	31.29	11.22

Sample No.	Rg40-1	Rg40-2	Rg40-3	Rg40-4	Rg40-5	Rg42-1	Rg42-2	Rg42-4	Rg42-5	Rg55-1	Rg55-2	Rg55-3
SiO_2	73.02	73.54	73.07	73.1	73.92	74.38	73.26	74.65	74.45	71.01	73.19	73.13
TiO_2	0.21	0.22	0.21	0.21	0.21	0.16	0.19	0.16	0.17	0.21	0.19	0.19
Al_2O_3	14.59	14.57	14.77	14.11	14.37	13.82	14.26	13.74	13.79	13.68	13.97	13.87
TFe_2O_3	1.38	1.48	1.42	1.51	1.22	1.04	1.29	1.02	1.16	1.70	1.45	1.48
FeO	0.30	0.31	0.42	0.28	0.63	0.25	0.48	0.55	0.49	0.49	0.39	0.44
MnO	0.02	0.02	0.01	0.03	0.02	0.03	0.02	0.01	0.02	0.01	0.01	0.01
MgO	0.15	0.15	0.10	0.13	0.15	0.15	0.19	0.13	0.16	0.34	0.21	0.25
CaO	0.69	0.38	0.61	0.55	0.40	1.21	1.05	1.03	1.02	1.34	0.98	1.02
Na_2O	3.14	2.90	2.48	2.71	3.45	3.60	3.12	3.45	3.46	3.25	3.67	3.08
K_2O	4.73	4.74	4.81	4.72	4.47	4.60	5.01	4.72	4.78	4.75	4.37	5.22
P_2O_5	0.06	0.06	0.06	0.06	0.05	0.04	0.05	0.04	0.04	0.06	0.05	0.05
LOI	2.02	1.93	2.46	2.29	1.67	0.92	1.54	1.03	0.94	3.60	1.37	1.69
σ	2.06	1.91	1.77	1.83	2.03	2.14	2.18	2.11	2.16	2.28	2.14	2.29
Li	24.30	23.40	24.40	25.20	21.90	10.90	13.40	9.57	8.86	9.72	8.91	8.99
Be	1.65	1.53	1.24	1.17	1.56	2.11	1.87	2.00	2.04	1.54	1.46	1.37
Sc	2.43	2.26	2.17	2.35	2.16	2.17	2.27	1.95	2.64	3.39	2.14	2.66
V	16.4	13.2	12.1	12.1	12.4	9.16	9.16	7.97	11.3	24.8	16.9	18.8

Continued Table 3

Sample No.	Rg40-1	Rg40-2	Rg40-3	Rg40-4	Rg40-5	Rg42-1	Rg42-2	Rg42-4	Rg42-5	Rg55-1	Rg55-2	Rg55-3
Cr	10.3	20	5.78	17.4	2.28	8.16	7.12	1.9	7.26	6.12	2.6	4.36
Co	2.06	1.68	1.99	3.18	2.19	1	1.26	0.751	1.14	2.87	2.05	2
Ni	4.69	8.73	2.84	8.14	1.6	3.47	2.92	0.72	2.39	4.15	3.55	3.88
Ga	16.9	15.9	16.6	15.2	15.3	16.3	16	16.6	17.4	18	16.2	15.6
Rb	103	103	101	94.9	97.9	109	112	110	112	119	71.3	101
Sr	241	233	204	235	222	211	219	188	218	258	259	242
Y	8.07	7.49	8.05	7.98	7.9	9.31	9.9	8.45	6.94	9.52	6.06	8.17
Zr	124	123	126	111	114	101	123	104	120	119	101	109
Nb	10.3	11.3	10.3	12.2	12.8	10.6	11.5	10.9	8.96	11.9	11.9	12.7
Cs	1.28	1.2	1.79	1.11	1.14	1.15	1.02	0.896	0.872	1.08	0.647	1.28
Ba	1347	1329	1331	1313	1115	949	1204	846	1021	1276	1128	1227
La	27.7	27	28.2	26.1	22.2	25.3	35.1	19.9	27.6	23.3	10.2	14
Ce	46.8	44.2	46.5	43.9	42.5	43.1	59.3	34	47.6	38.7	18.1	24.5
Pr	4.96	4.66	4.92	4.7	4.14	4.51	5.92	3.62	5.02	4.09	1.89	2.51
Nd	17.2	16.4	17	16.1	14.4	15.3	19.9	12.4	17	13.9	6.4	8.63
Sm	2.78	2.51	2.58	2.42	2.4	2.62	2.86	2.23	2.57	2.41	1.11	1.52
Eu	0.597	0.467	0.514	0.53	0.576	0.491	0.52	0.466	0.561	0.516	0.238	0.331
Gd	2.07	2.04	1.96	1.89	1.85	2.09	2.49	1.75	2.08	2.05	1.14	1.47
Tb	0.301	0.288	0.281	0.289	0.28	0.327	0.344	0.279	0.274	0.326	0.184	0.241
Dy	1.4	1.27	1.33	1.31	1.4	1.59	1.62	1.4	1.28	1.67	0.909	1.24
Ho	0.26	0.219	0.238	0.244	0.231	0.302	0.302	0.26	0.198	0.338	0.205	0.265
Er	0.675	0.638	0.634	0.722	0.723	0.795	0.818	0.673	0.548	0.888	0.582	0.764
Tm	0.11	0.094	0.123	0.111	0.126	0.138	0.149	0.111	0.093	0.157	0.109	0.141
Yb	0.681	0.666	0.673	0.665	0.749	0.81	0.898	0.746	0.518	0.935	0.726	0.83
Lu	0.109	0.103	0.12	0.123	0.119	0.144	0.14	0.111	0.096	0.14	0.119	0.131
Hf	3.9	3.9	3.88	3.58	3.67	3.12	3.73	3.15	3.53	3.44	3.2	3.15
Ta	0.701	0.458	0.751	1.35	1.1	0.709	0.993	0.851	0.409	0.819	0.957	0.98
Pb	25.3	28.4	28.4	27.5	23.8	33.2	31.8	29.5	31.9	26.3	23.9	26.5
Th	2.69	2.74	2.88	2.63	3.18	3.29	3.71	2.9	3.12	4.62	3.76	4.24
U	0.821	0.67	0.769	0.859	0.786	0.469	0.544	0.629	0.525	0.686	0.613	0.79
$(La/Sm)_N$	6.27	6.77	6.88	6.78	5.82	6.07	7.72	5.61	6.76	6.08	5.78	5.79
$(La/Yb)_N$	27.42	27.33	28.25	26.46	19.98	21.06	26.35	17.98	35.92	16.80	9.47	11.37

Note: Major elements are analyzed using XRF (in wt%), trace elements using ICP-MS (in ppm)

considered to be Permian in age, and samples from the Dairigen valley (ZH7 and ZH15) were interpreted as Precambrian plutons in the Diebusige complex. However, zircons from those plutons are euhedral and prismatic, with well-developed oscillatory zoning and high Th/U ratios, indicating a magmatic origin. Therefore, these ages represent the zircon crystallization ages and the emplacement ages of the plutons. The laser ablation inductively coupled plasma mass spectrometry (LA-ICP MS) U–Pb zircon analyses in this study yielded ages of 325–348 Ma, thus constraining the emplacement ages of these samples as early Carboniferous (Mississippian). In addition, many previous studies have reported early Carboniferous plutons in the Langshan region (Fig. 2). Dan et al. (2016) reported coeval monzogranites (337–346 Ma) south of the Dabashan pluton and the Diebusige complex, called the “Diebusige pluton” and “south Diebusige pluton”, respectively (see locations in the Fig. 2a). Moreover, mafic plutons with similar ages have been reported in the northwestern Langshan (around Chaoge Ondor). Liu et al. (2016a) reported early Carboniferous mafic plutons in the west of Chaoge Ondor, including quartz diorite (338 Ma), olivine gabbro (327 Ma), and tonalite (325 Ma) plutons. In the north of Chaoge Ondor, Wang et al. (2015) found gabbros (328 Ma) and gabbro-diorites (320 Ma). Our study, together with previous data, shows that the early Carboniferous was an important magmatic period in the northeastern Alxa block. In addition, early Carboniferous plutons in the Diebusige complex provide new information on the timing of the Diebusige complex, which has generally been considered as Precambrian basement in the western block of the North China Craton. Therefore, these early Carboniferous plutons in the Langshan region could provide key information on the geodynamic evolution of the southern CAOB.

5.2 Petrogenetic classifications

Previous studies have proposed various classification schemes for granitoids. For example, Chappell and White (1974) proposed I-type and S-type genetic classifications based on the Caledonian Lachlan Fold belt granitoids in SE Australia, and this scheme has been widely used in recent decades. Barbarin (1999) divided granitoids into several types according to their mineral assemblages, their field and petrographic features, and their chemical and isotopic characteristics, such as muscovite-bearing peraluminous granitoids, arc tholeiitic granitoids, and peralkaline and alkaline granitoids. Based on geochemical studies on Scottish Caledonian granitoids, Tarney and Jones (1994) proposed a new concept of high Ba–Sr granitoids, which exhibit high Sr (> 300 ppm) and Ba (> 500 ppm) contents, distinct from the low Ba–Sr values that characterize I-, S-, and A-type granites of the Phanerozoic (Chappell and White, 1992). High Ba–Sr granitoids share some common geochemical features, including: (1) high contents of LILEs such as Ba, Sr, and K_2O; and (2) crust-like isotopic compositions (Tarney and Jones, 1994; Fowler and Rollinson, 2012; Peng et al., 2013).

The Dabashan plutons display high Ba (823–2817 ppm) and Sr (166–520 ppm) contents and high K/Rb ratios (315

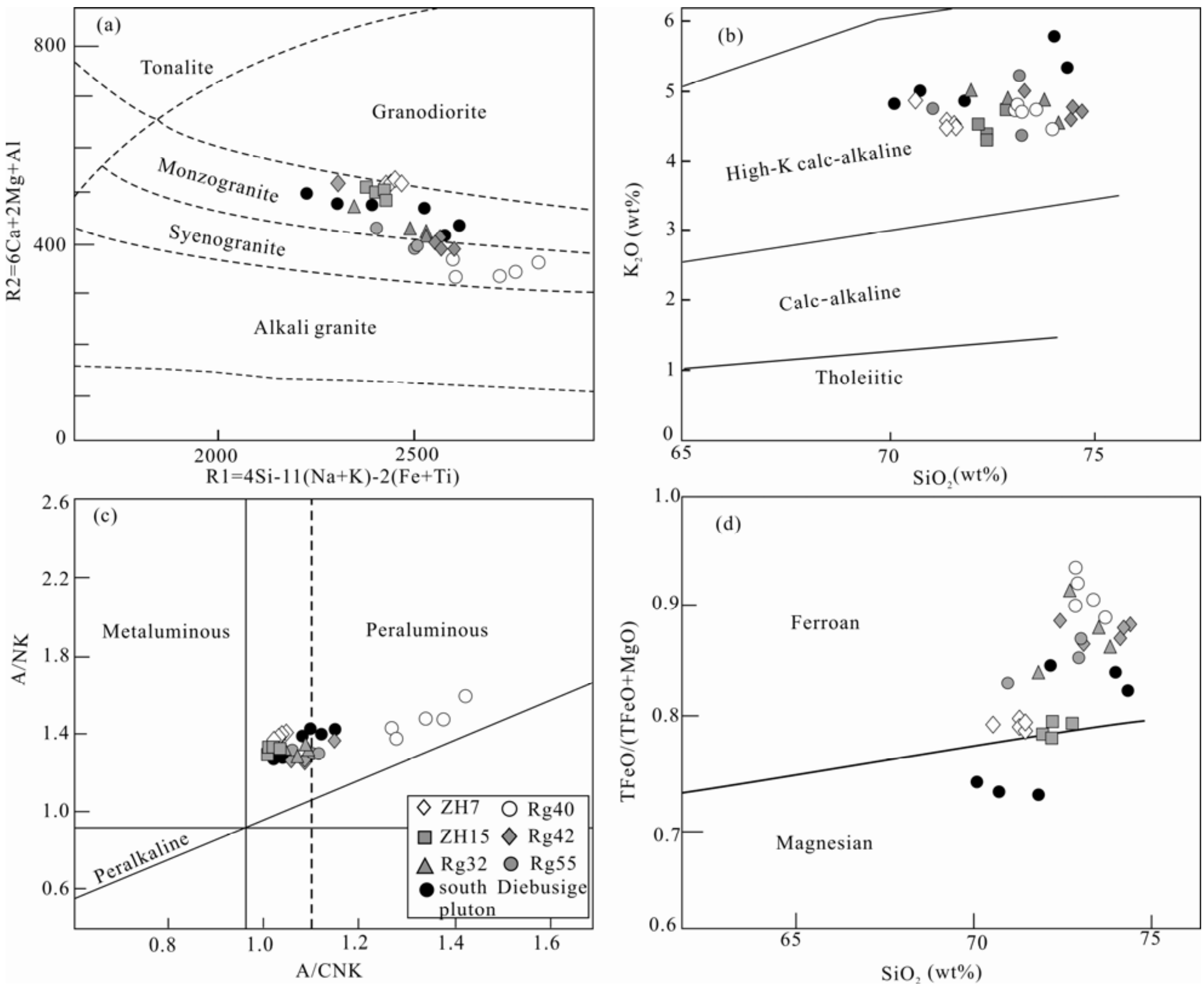

Fig. 7. (a) R2 vs. R1 diagram (after De la Roche et al., 1980), R1= [4Si-11(Na+K)-2(Fe+Ti); R2= (Al+2Mg+6Ca); (b) K_2O vs. SiO_2 diagram (after Peccerillo and Taylor, 1976);(c) A/NK vs. A/CNK diagram (after Maniar and Piccoli, 1989), A/CNK = mol $Al_2O_3/(Na_2O+K_2O+CaO)$, A/NK = mol $Al_2O_3/(Na_2O+K_2O)$; (d) TFeO/(TFeO + MgO) vs. SiO_2 discrimination diagrams (after Frost et al., 2001) for the Dabashan pluton in the southern Langshan.

–627), but low Rb/Ba ratios (0.02–0.14), and exhibit fertile zircon Hf isotopic compositions [$\varepsilon_{Hf}(t)$=−14 to −20] and whole-rock Sr–Nd isotopic compositions [$\varepsilon_{Nd}(t)$=−18 to −19, Dan et al., 2016]. All of the above geochemical characteristics are comparable to those of typical high Ba–Sr granitoids (Tarney and Jones, 1994). Although some samples exhibited lower Sr concentrations than those of the original definitions of Tarney and Jones (1994), they evolve toward high Ba, similar to the West Scottish Caledonian high Ba–Sr granitoids, but totally different from normal low Ba–Sr-type granitoids (e.g., East Scottish Caledonian granitoids) in the Sr–Rb–Ba plot (Fig. 10). Moreover, Dabashan plutons exhibit strong REE fractionation patterns, obvious depletion of Nb, Ta, P, and Ti (Fig. 9), and especially low Y and Yb contents coupled with high Sr/Y and La/Yb ratios, which are also comparable to the characteristics of typical of high Ba–Sr granites (Tarney and Jones, 1994; Fowler et al., 2008; Ye et al., 2008; Choi et al., 2009; Peng et al., 2013; Liu et al., 2017). In addition, we reevaluated data from the Diebusige and south Diebusige plutons in the study by Dan et al. (2016), named the south Diebusige pluton in this study, and found that those granite samples also displayed similar geochemical characteristics to those of high Ba–Sr granites, such as high Ba (2119–2877 ppm) and Sr (276–476 ppm) concentrations. They were also alkali-rich, with high K_2O contents and high K_2O/Na_2O ratios (>1), and were enriched in LILEs and LREEs. Moreover, they exhibited fertile whole-rock Sr–Nd and zircon Hf isotopic compositions (Dan et al., 2016). Therefore, all the Mississippian granitoids in the southern Langshan, including the Dabashan and south Diebusige plutons, should be high-K calc-alkaline, high Ba–Sr granites.

5.3 Nature of magma sources

All the high Ba–Sr granites in southern Langshan exhibit high SiO_2 and K_2O, and A/CNK and K_2O/Na_2O ratios (mostly >1), as well as low MgO, Cr, and Ni concentrations, which imply that crustal sources may have played important roles in their formation processes. These granites have crust-like isotopic compositions, including zircon Hf isotopes and whole-rock Sr–Nd isotopes.

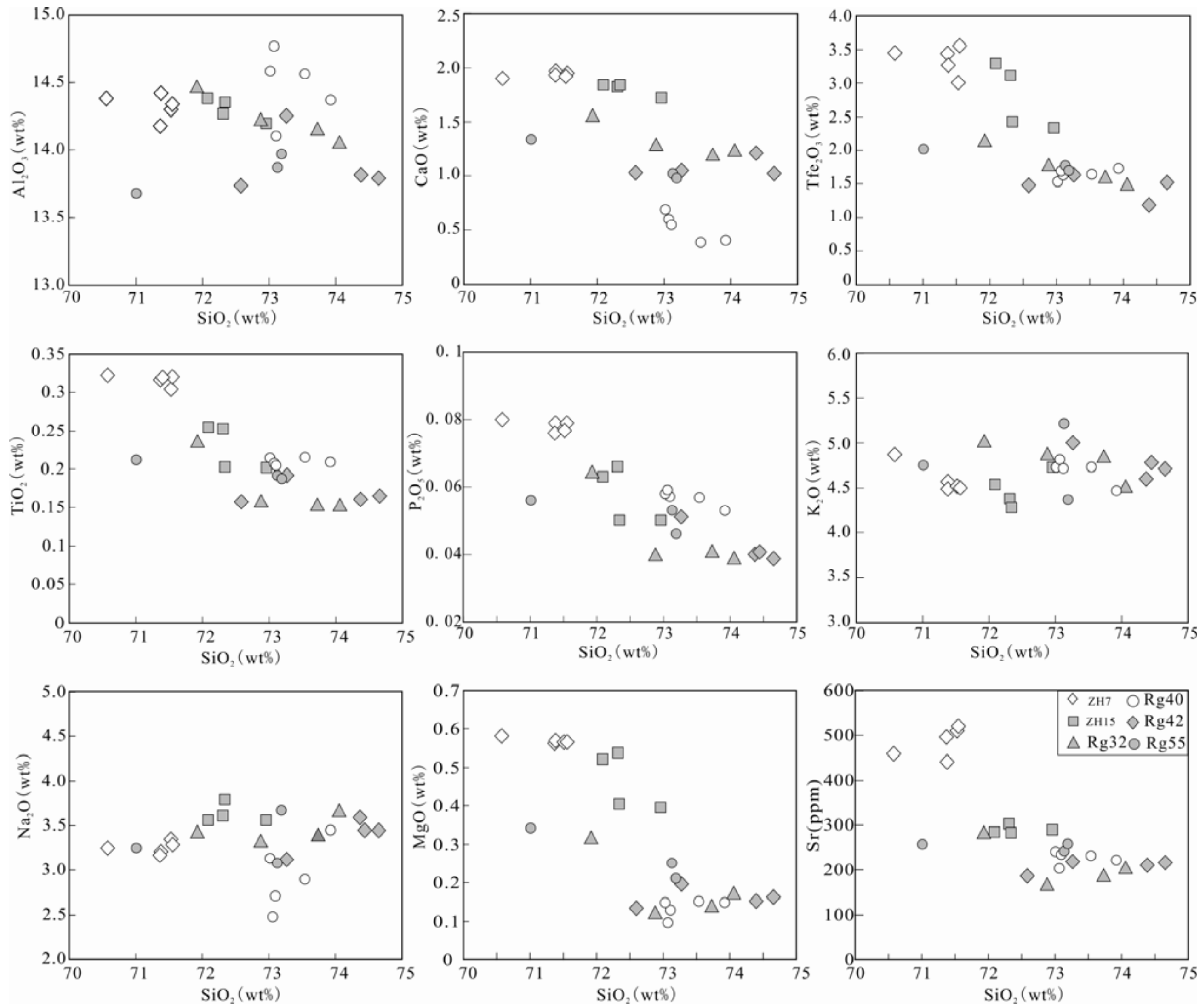

Fig. 8. Harker variation diagrams for Dabashan pluton in the southern Langshan.

Specifically, they exhibit extremely low zircon $\varepsilon_{Hf}(t)$ values (from −20.3 to −13.9), and old T_{DM2} (2213–2610 Ma). In addition, they also exhibit low $\varepsilon_{Nd}(t)$ values (from −19.1 to −18.0), and old T_{DM2} (2558–2657 Ma). The old two-stage Nd and zircon Hf isotopic model ages are similar to the ages of the Diebusige TTGs (our unpublished data). Thus, their fertile isotopic compositions imply that the Diebusige TTG may have played an important role in the generation of these high Ba–Sr granites.

These high Ba–Sr granites in southern Langshan exhibit diagnostic high Ba and Sr contents, which indicate a high Ba–Sr source in addition to the Diebusige complex. Previous studies have shown that pelagic sediments commonly have enhanced Ba (thousands of ppm) and Sr (thousands of ppm), and are invariably LREE-enriched (La/Yb ca. 10; Plank and Langmuir, 1998; Fowler et al., 2008). Therefore, pelagic sediments are inferred to be a main material source of Ba and Sr in the generation of such high Ba–Sr granites. Similar to the Setouchi sanukitoids, they exhibit consistent Sm/La ratios with increasing Th/La ratios (Fig. 11a), which imply that the subducted sediment-derived component is the major metasomatic agent for their generations (Tatsumi, 2006). In the $(La/Sm)_N$ versus Ba/Th diagram, all the high Ba–Sr granites display a "sediment involvement" trend, which indicates the addition of an oceanic sedimentary component (Fig. 11b). In comparison with typical high Ba –Sr granites, the high Ba–Sr granites in the southern Langshan area exhibit relatively lower Sr abundances, but some have higher Ba contents (up to 2000 ppm). As Ba is linked to both biogenic barite and hydrothermal components, and Sr is linked to carbonate phases (Plank and Langmuir, 1998), we propose that carbonate phases are minor components in these pelagic sediments. This conclusion is consistent with insignificant roles of carbonate metasomatism in their generations (Fig. 11c). All these lines of evidence confirm the involvement of subducted sediment components in the source magma of the high Ba–Sr granites in southern Langshan.

In addition, the early Carboniferous high Ba–Sr granites in southern Langshan exhibited higher K_2O/Na_2O ratios

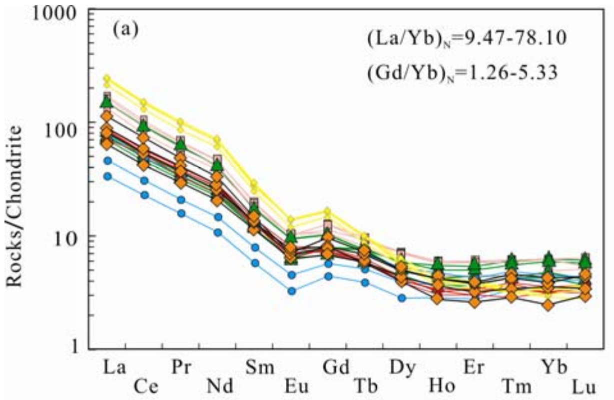

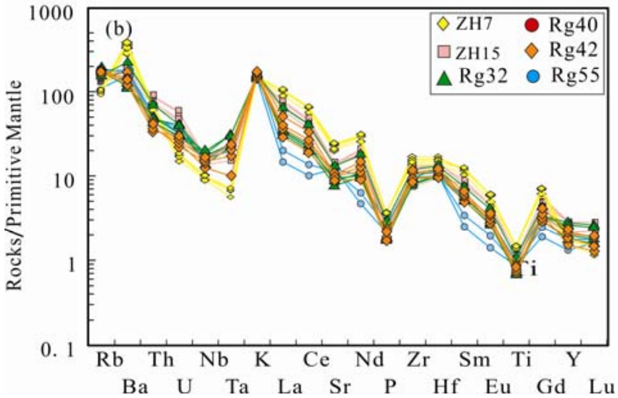

Fig. 9. The Chondrite-normalized REE pattern of the Dabashan pluton in the southern Langshan (normalized data and N-MORB values are from Sun and McDonough, 1989).

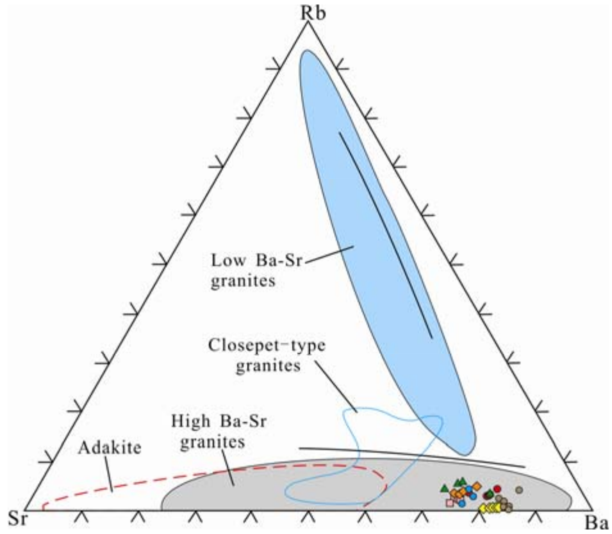

Fig. 10. Sr–Rb–Ba plot of the Dabashan pluton in the Southern Langshan (after Tarney and Jones, 1994; Peng et al., 2013 and references therein).
Data of south Diebusige are from Dan et al., 2016. Symbols are as in Fig. 9.

than those of the Diebusige complex. Experimental petrological data have shown that amphibolite-facies sodic TTGs could not produce melts with sufficient K_2O to account for potassic granites (Watkins et al., 2007). Therefore, the high Ba–Sr granites could not be derived directly from partial melting of Diebusige TTG. In addition, the high K_2O content should not result from fractionation because of the absence of positive correlation between SiO_2 and K_2O contents (Fig. 8), ruling out causes of the AFC process. Mechanisms have been proposed to account for the potassium-rich nature of the high Ba–Sr granites. Peng et al. (2013) proposed that terrigenous sediments with high K_2O/Na_2O could generate the amount of K_2O required for the generation of high Ba–Sr granites (Plank and Langmuir, 1998). Moreover, studies of arc magmas have revealed that fluids released from a subducting slab are also enriched in alkali elements, LILEs and LREEs, which could provide potassium-rich volatile-bearing phases in the mantle source (Peng et al. 2013 and references therein). However, all these high Ba–Sr granites exhibited relatively high $(Hf/Sm)_{PM}$ values (1.19–4.14), similar to those of volcanic arc basalts extracted from a mantle source metasomatized by subduction-related melt (Fig. 11 c, La Flèche et al., 1998). Therefore, it is more likely that terrigenous sediment melts provided sufficient K_2O rather than subduction-related fluids.

Moreover, high Ba–Sr granites in southern Langshan exhibited strongly fractionated REE patterns, highly enriched LREEs, and depleted HREEs. In the Sr/Y versus Y plot (Fig. 11d), all high Ba–Sr granites display an evolutionary trend from partial melting of eclogite (Drummond and Defant, 1990), indicating garnet residues in their sources.

Therefore, ancient crustal materials and subducted sediments both played important roles in the generation of high Ba–Sr granites in southern Langshan. Taking their fertile isotopic compositions into account, strongly fractionated REEs, highly enriched LREEs, and depleted HREEs, we propose that their parental magma originated from partial melting of highly-enriched mantle at high pressures with garnet residue in the source material.

5.4 Fractional crystallization process

Some major and trace elements of high Ba–Sr granites in southern Langshan display covariation trends against SiO_2 (Fig. 8), which may have resulted from partial melting of a metabasaltic source to different degrees, fractional crystallization of a common parental magma, or binary magmatic mixing (Jiang and Li, 2014). Distinction between fractional crystallization and batch partial melting can be made graphically using incompatible trace elements with different bulk solid melt partition coefficients *D* (Schiano et al., 2010). In the Th–Th/Nd diagram (Fig. 12a), the high Ba–Sr granites display almost horizontal lines, similar to that of the fractional crystallization trend. High Ba–Sr granites show roughly positive correlations between La/Yb and Dy/Yb ratios (Fig. 12b), which are different from trends resulting from dehydration melting of hydrous minerals such as biotite and amphibole (Jiang and Li, 2014). In addition, there have not been mafic microgranular enclaves (MME) reported in the high Ba–Sr plutons based on our data and those of Dan (2016). These high Ba–Sr granites have few zircon xenocrystals with Precambrian ages (Fig. 5). In general, they display limited whole-rock major and trace element and Sr–Nd isotopic compositions (Dan et al.,

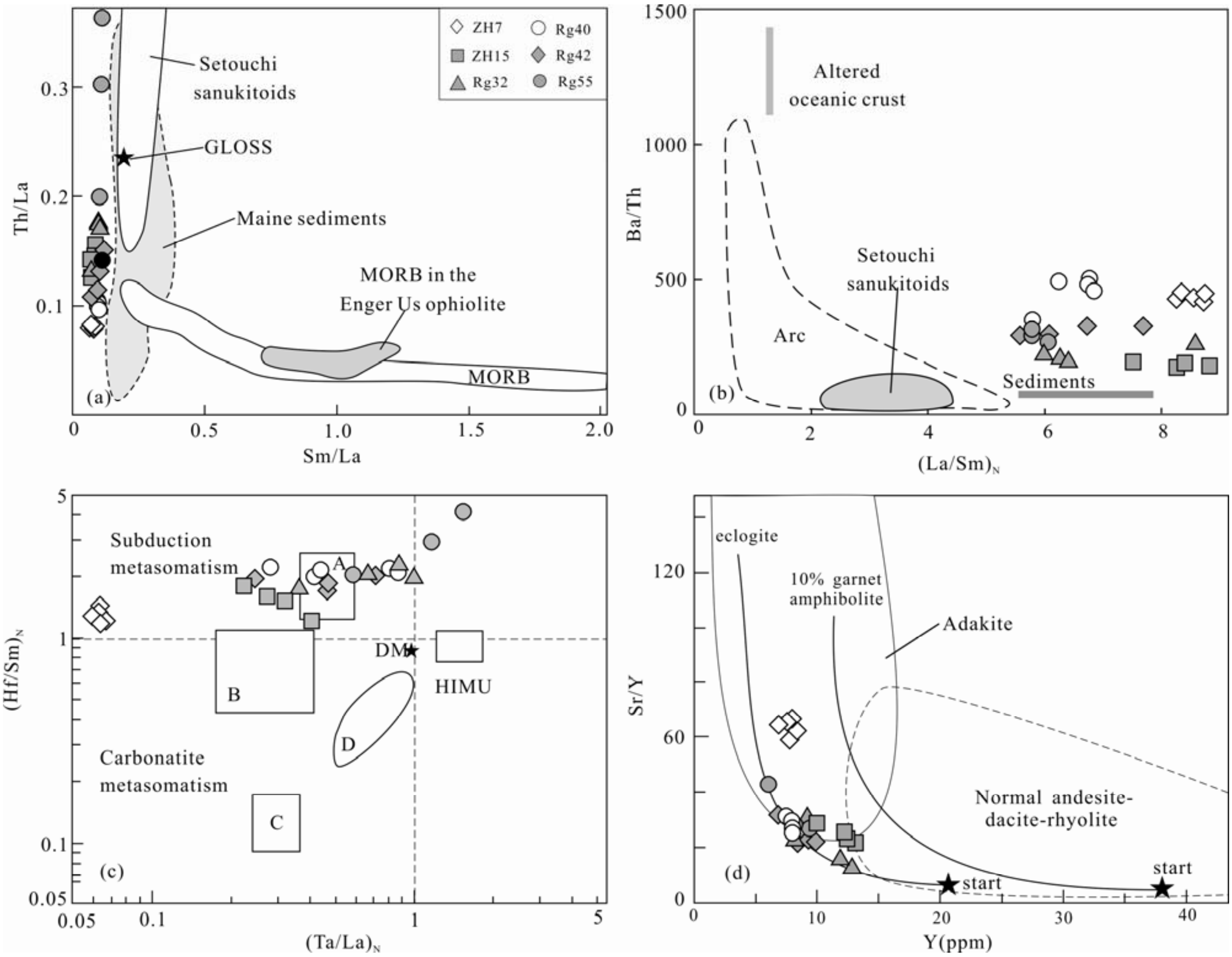

Fig. 11. (a) Sm/La versus Th/La diagram (modified from Plank, 2005); (b) $(La/Sm)_N$ versus Ba/Th diagram (modified from Tatsumi, 2006); (c) $(Ta/La)_{PM}$ versus $(Hf/Sm)_{PM}$ diagram (modified from La Flèche et al., 1998 and references therein), A–volcanic arc basalts extracted from a mantle source metasomatized by silicated fluids; B–volcanic arc basalts extracted from an hydrated mantle source; C–carbonatitic lavas; E–Alkalic basalts interpreted to have been produced by a lithospheric mantle source metasomatized by carbonatites; (d) Y versus Sr/Y diagram (Defant and Drummond, 1990). Data of MORB in the Enger Us ophiolite are from Zheng et al. (2014). Partial melting curves for basalt leaving residues of eclogite and garnet (10%) amphibolite from Drummond and Defant (1990) .

2016), and exhibit fairly homogeneous zircon Hf isotopic compositions (Fig. 6). Thus, magma mixing and/or AFC (assimilation of crustal materials associated with fractional crystallization) processes can be ruled out. Therefore, we consider fractional crystallization to be the major mechanism responsible for chemical variations of high Ba–Sr granites in southern Langshan.

Negative correlations between SiO_2 and cafemic components (Fig. 8), such as total Fe_2O_3, MgO, CaO, MnO, and TiO_2, suggest fractionation of hornblende and the principal ferromagnesian phase from the magmas. Because hornblende is the major host mineral of middle REEs, the inference of hornblende-dominated fractionation is also confirmed by positive correlations between Er and Dy (Fig. 12), which indicate that the original magma may have been derived from water-rich sources. On the Rb/Sr and Ba versus Sr diagrams, a sharp increase in Ba and Rb/Sr ratios with decreasing Sr concentrations suggests fractionation of K-feldspar and plagioclase (Fig. 12c–d). The Al_2O_3 and CaO contents decrease with increasing SiO_2 contents, which indicates plagioclase fractionation from the magma. This inference is also supported by variable depletions in Sr and Eu in the primitive mantle-normalized trace element diagram (Fig. 9). However, concomitant fractionation of plagioclase and hornblende could bring strong negative Sr anomalies without potential Eu anomalies (Chen et al., 2000; Zhang et al., 2009), which is not the case for the high Ba–Sr granites. We propose that plagioclase fractionation was likely insignificant. Moreover, the lack of obvious correlation between SiO_2 and Sr also supports this conclusion. In the $(La/Yb)_N$ vs. La diagram (Fig. 12f), fractionation of allanite and monazite plays an important role in the variation of REEs contents. Apatite also played an important role in magmatic evolution, based on negative correlations between P_2O_5 and SiO_2 (Fig. 8).

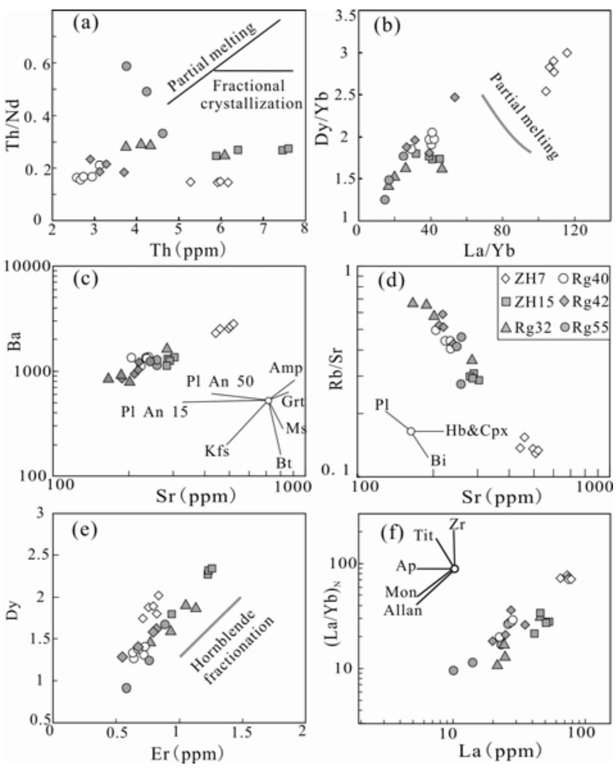
Fig. 12. Element variation diagrams of (a) Th/Nd vs. Th (modified from Schiano et al., 2010) (b) Dy/Yb vs. La/Yb, (c) Ba vs. Sr, (d) Rb/Sr vs. Sr, (e) Dy vs. Er, (f) La/Yb)N vs. La for Dabashan pluton in the southern Langshan, showing that fractional crystallization is responsible for chemical variations.

In summary, fractional crystallization played an important role in the formation of high Ba–Sr granites in the southern Langshan. Hornblende, K-feldspar, apatite, allanite, and monazite fractionated from the original magma.

5.5 Tectonic and petrogenesis implications

The evolutionary process of the paleo-ocean plays an important role in recognizing the tectonic implications of high Ba–Sr granites in the southern Langshan. Ophiolites and/or ophiolitic mélanges represent fragments of the upper mantle and oceanic crust, and are usually considered to be remains of accreted fragments of vanished oceans and of material that was deposited in the subducted trenches (Xiao et al., 2014). Two ophiolitic mélanges have been reported in the Alxa region: the Enger Us and Quagan Qulu ophiolites (Fig. 1b). The Enger Us ophiolite occurs in the NEE of the Enger Us fault belt as large-scale mélange accumulations, mainly composed of ultramafic and mafic rocks, with a matrix comprising highly deformed Carboniferous clastic rocks and tuffs (Wang et al., 1994; Zheng et al., 2014). Massive and pillow basalts in the Enger Us ophiolite exhibit N-MORB geochemical affinities, and are characterized by depletions of LREEs without fractionations of high field strength elements (HFSEs) and negative Nb–Ta anomalies. It is inferred that the magmas of these rocks were derived from a depleted mantle source in a mid-ocean ridge setting (Zheng et al., 2014). Gabbros of the Enger Us ophiolites exhibit K–Ar isotope and zircon U–Pb ages of 356 Ma and 380 Ma, respectively (Wang et al., 1994). Zircons from a pillow lava sample yielded a SHRIMP zircon U–Pb age of 302±14 Ma (Zheng et al., 2014). Moreover, recent studies reported late Permian radiolarians in cherts of the Enger Us ophiolite (Xie et al., 2014). Gabbros in the Quagan Qulu ophiolite show high MgO contents, compatible elements, and Al_2O_3/TiO_2 ratios, but low TiO_2 and SiO_2 contents. They are enriched in LILEs and depleted in LREEs and HFSEs, indicating a SSZ-type ophiolite (Zheng et al., 2014). Zircons in a gabbro sample from the Quagan Qulu ophiolite yielded a SHRIMP zircon U–Pb age of 275±3 Ma. These geochemical and geochronological data from ophiolites in the Alxa region, together with structural analysis in the Enger Us fault (Wang et al., 1998), all indicate that the southward-dipping paleo-ocean subduction process may have continued from the late Devonian to the late Carboniferous –early Permian, and the final closure of the Paleo-Asian Ocean may have taken place later than the early Permian.

In the Langshan region, late early Carboniferous mafic plutons (338–320 Ma, Wang et al., 2015; Liu et al., 2016a) display calcic, metaluminous to weakly peraluminous characteristics, and are characterized by enrichment in LREEs and LILEs and depletion in HREEs and HFSEs. They exhibit variable zircon $\varepsilon_{Hf}(t)$ values (from −6.9 to 2.0), and old T_{DM2}(1218–1783 Ma). Their whole-rock $\varepsilon_{Nd}(t)$ values are also variable (from −6.9 to −0.4), which suggests that they may have originated from the subduction-modified continental lithospheric mantle (Wang et al., 2015). It has been suggested that those late Carboniferous mafic plutons may have formed in a continental magmatic arc setting related to the subduction of the Paleo-Asian Ocean plate (Liu et al., 2016a).

Two ductile deformations were found at the eastern boundary of the Alxa block, especially in the Langshan region, including a ductile sinistral shear belt that outcrops along the present boundary between the mountains and the Cenozoic Jilantai-Hetao graben (Fig. 2b), and deformation related to the overlying westward thrusting, which is more prominent in the western part of the mountains. The deformation time of the upper westward thrusting along the eastern boundary of the Alxa block can be constrained to ca. 351 Ma (Zhang et al., 2013a), and is considered to be the result of interactions between the NCC and the Alxa block (Zhang et al., 2013a). Syntectonic muscovites from mylonitic quartz schist in the NE-trending sinistral shearing belt yielded plateau ages of 356.7±2.5 Ma and 379±4.7 Ma, respectively, which imply that the sinistral shearing occurred before the late Devonian (Gong et al., 2017). Some studies have proposed that this NE-trending sinistral shearing belt is related to Paleo-Asian Ocean subduction processes (Gong et al., 2017). As the sinistral shear cut the westward thrust in the Bayanbulage region, we infer that the sinistral shear is younger than the westward thrusting (Zhang et al., 2013a). Structural analysis data in the Langshan region indicate an approximately EW compressive event with lateral ductile sinistral shearing during the early Carboniferous in the Langshan region.

Data from ophiolites and mafic plutons in the Alxa region, combined with structural analysis, all demonstrate the existences of paleo-ocean subduction from the late Devonian to early Permian (Feng et al., 2013; Lin et al., 2014; Xiao et al., 2015, 2018). Thus, these early Carboniferous high Ba–Sr granites in southern Langshan are interpreted to have formed in a subduction environment.

Previous studies have proposed various petrogenetic mechanisms to account for the special geochemical characteristics of high Ba–Sr granitoids, including: (a) the hydrous melting of crust underplated by mafic magmas with the same characteristics; (b) the partial melting of lower lithosphere that had been metasomatized by small-volume asthenospheric carbonatitic melts; (c) the partial melting of mafic lower crustal rocks associated with the mingling of enriched mantle-derived intermediate (enclave) magmas (Ye et al., 2008; Choi et al., 2009; Zhang et al., 2015); (d) crystal fractionation of shoshonitic mafic magmas originating from an enriched lithospheric mantle (Liu et al., 2017); and (e) derivation from a highly enriched mantle source that was metasomatized by subduction-related fluids and/or melts (Peng et al., 2013).

Tarney and Jones (1994) proposed that high Ba, Sr and P contents could result from penetration of the lower lithosphere by small-volume asthenospheric carbonatitic melts. However, our samples exhibit relatively lower Sr abundances (400 ppm), but higher Ba contents (up to 2000 ppm; Table 3) in comparison with typical high Ba–Sr granites (Tarney and Jones, 1994). Those characteristics, together with low P_2O_5 abundances, are all inconsistent with an origin related to carbonate metasomatism. Moreover, carbonatitic metasomatism would result in systematic depletion of HFSEs (Hf and Ta) relative to REEs (Sm and La), because REEs are much more soluble than HFSEs in carbonatitic melts (La Flèche et al., 1998 and references therein). All of the samples exhibit relatively high $(Hf/Sm)_{PM}$ values (1.19–4.14), which are notably higher than those of typical carbonatitic lavas (0.2; La Flèche et al., 1998). Therefore, carbonatitic melts may not have participated in the genesis of these high Ba–Sr granites in the southern Langshan.

Contemporary mafic rocks in the Langshan region display different geochemical characteristics from those of high Ba–Sr granites. All of these mafic plutons, including gabbros, gabbro-diorites, quartz diorites, and olivine gabbros, are sodic with high Na_2O/K_2O ratios (>1, Wang et al., 2015; Liu et al., 2016a), and display calc-alkaline–tholeiitic characteristics. These mafic plutons characteristically exhibit relatively low Ba and Sr contents (Wang et al., 2015; Liu et al., 2016a). In addition, these mafic plutons have notably different isotopic compositions. Carboniferous mafic plutons typically exhibit weak fertile isotopic compositions with variable zircon $\varepsilon_{Hf}(t)$ values (−6.9 to 2.0, Liu et al., 2016a), and whole-rock $\varepsilon_{Nd}(t)$ values (from −0.4 to −4.5, Wang et al., 2015). In contrast, high Ba–Sr granites exhibit much more evolved isotopic compositions, and have extremely low whole-rock $\varepsilon_{Nd}(t)$ values (from −18.0 to −19.1, Dan et al., 2016) and zircon $\varepsilon_{Hf}(t)$ values (from −23.1 to −13.0). Therefore, it is not possible for high Ba–Sr granites to be derived from hydrous melting of crust underplated by contemporary mafic magmas because of their different geochemical characteristics.

Magmatic rocks generated by fractional crystallization processes generally exhibit a continuous compositional trend from basaltic rocks to felsic rocks. In contrast, there is an obvious SiO_2 gap between contemporary mafic plutons and high Ba–Sr granites (Wang et al., 2015; Liu et al., 2016a). All the mafic plutons have low K_2O+Na_2O contents, and display calc-alkaline–tholeiitic rather than shoshonitic characteristics. Moreover, mafic plutons have obviously different Sr–Nd–Hf isotopic compositions, which cannot be changed during fractional crystallization processes. Therefore, high Ba–Sr granites may experience some degrees of fractional crystallization during the ascent of their parent magmas, but cannot be generated by fractional crystallization of contemporary calc-alkaline–tholeiitic mafic rocks.

Based on our observations and data from Dan (2016), no mafic microgranular enclaves (MMEs) were found in the high Ba–Sr granites. High Ba–Sr granites formed by magma mixing between mafic and silicic end member typically host numerous MMEs, such as high Ba–Sr granites in the British Caledonian province (Fowler et al., 2001), the northwestern margin of the Tibetan Plateau (Ye et al., 2008), and Central Mongolia (Zhang et al., 2015). Based on their consistent geochemical compositions, such as their limited Sr, Nd isotopes, and zircon Hf isotopes, it is not possible that magma mixing has played a dominant role in the generation of these high Ba–Sr granites. Consequently, an origin from partial melting of an enriched SCLM metasomatized by subduction-related sedimentary melts and/or fluids is considered below.

The high Ba–Sr granites emplaced into the Diebusige complex (Fig. 3) form Precambrian basement in the southern Langshan. In addition, their fertile isotopic compositions indicate that ancient crustal materials might have played important roles in their genesis. In addition, high Sr and Ba contents and potassic characteristics imply that subducted sediments were also important source materials. Therefore, we propose that the early Carboniferous high Ba–Sr granites in southern Langshan formed in a continental arc setting that resulted from the southward subduction of the Paleo-Asian Ocean. Detailed petrogenesis mechanisms are introduced below.

In the early Carboniferous, the Paleo-Asian Ocean crust (represented by the Enger Us ophiolite) was subducted southeastward beneath the Alxa block (present coordinates). Given that abundant geological and geophysical observations of sediment subduction indicate that most of the crustal material was transported by a subducted channel into the mantle (Kamber and Collerson, 2000; Scholl and Huene, 2007), we propose that pelagic sediments were brought to great depths in the subduction zone, and that partial melting occurred in the process of subduction. Subcontinental lithospheric mantle was metasomatized by those subducted sediment-related melts (stage 1 in Fig. 13). Dehydration of subducted oceanic crust during subduction resulted in partial melting of the metasomatized subcontinental lithospheric mantle wedge, and brought basaltic magmas (stage 2 in Fig. 13). In the

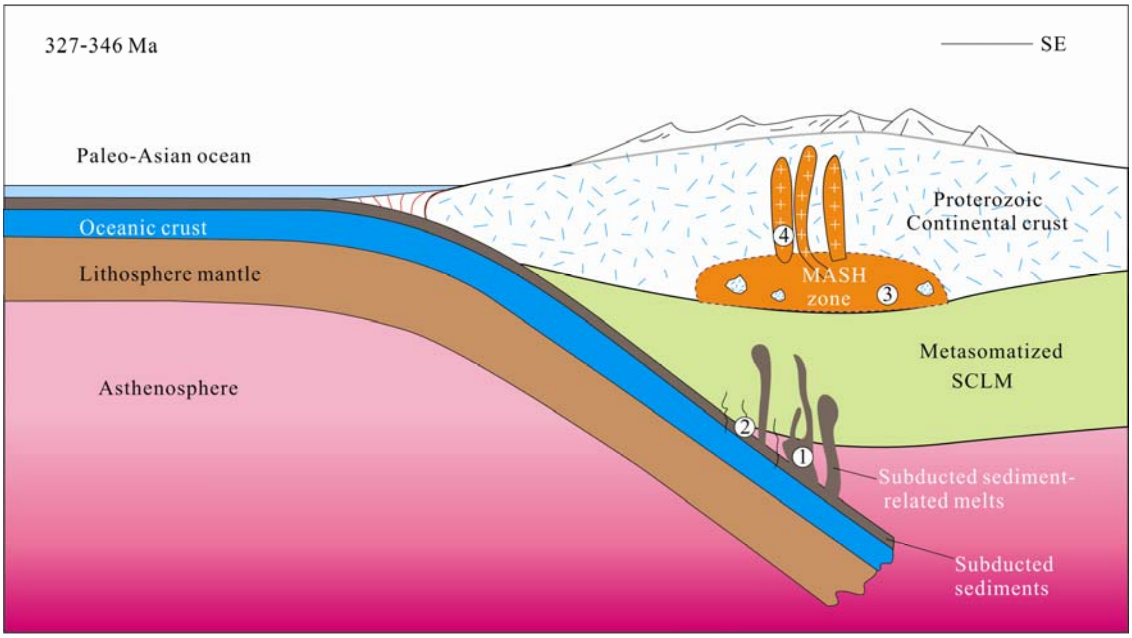

Fig. 13. The petrogenetic–tectonic model for high Ba-Sr granites in the southern Langshan (not scaled). See detailed discussions in the text.

lowermost crust or mantle–crust transition zone, basaltic magmas that ascend from the mantle wedge become neutrally buoyant, induce local melting, and assimilate and mix extensively (Hildreth and Moorbath, 1988), and melting, assimilation, storage, and homogenization (MASH) processes occur (stage 3 in Fig. 13). In the MASH zone, basaltic mantle magmas cause partial melting of ancient lower crust (possibly represented by the Diebusige complex), with which they hybridize and homogenize before rising and fractionating (Schwindinger and Weinberg, 2017). Magmas generated in the MASH zone ascended and were emplaced in the middle–upper crust at different depths (stage 4 in Fig. 13), which may have resulted in different geochemical characteristics, such as different Sr/Y and La/Yb ratios. Granite magma ascent in the crust evolves through multiple stages, with periods of intra-crustal magma interaction in felsic MASH zones (Schwindinger and Weinberg, 2017). Fractional crystallization occurred during the ascent, and hornblende, K-feldspar, apatite, allanite, and monazite fractionated from the original magma.

In terms of the regional geology, Carboniferous to Early Permian plutons are widely distributed along the northern margin of the North China Craton (NCC). Like the Dabashan pluton, they also intruded into Archean–Paleoproterozoic metamorphic rocks, and some of them were unconformably overlain by Jurassic–Cretaceous volcanic or sedimentary rocks (Zhang and Zhao, 2013). Recent geochronological data showed that the Carboniferous magmatism exhibited a peak age of 320 Ma at the northern margin of the NCC (Wang et al., 2015). In addition to their outcrops and ages, the Dabashan pluton and Carboniferous granitoids at the northern margin of the NCC all display crust-like geochemical characteristics, and exhibit fertile isotopic compositions, such as low $\varepsilon_{Nd}(t)$ and zircon $\varepsilon_{Hf}(t)$ values (Zhang et al., 2007, 2009; Zhang and Zhao, 2013). It is worth noting that some Carboniferous plutons at the northern margin of the NCC also exhibit high Ba and Sr abundances, such as the Hushiha pluton (Zhang et al., 2009). Some studies have proposed that these Carboniferous plutons formed in a continental arc during southward subduction of the Paleo-Asian Oceanic crust beneath the northern NCC (Zhang et al., 2007, 2009), which is consistent with the tectonic setting of the Dabashan pluton in this study. Based on spatial distributions, similar geochemical compositions, and tectonic settings, we propose that an active continental margin existed along the northern margins of the NCC and Alxa block in the Carboniferous. Furthermore, our data also imply that the Alxa block amalgamated to the NCC before the early Carboniferous.

6 Conclusion

(1) Zircon LA-ICP MS dating show that Dabashan plutons in the southern Langshan was crystallized in ca. 346–327 Ma, rather than in the Precambrian or Permian.

(2) Geochemical data indicate that those Mississippian granites in the southern Langshan belong to high Ba-Sr granites.They should be derived from a highly enriched mantle source metasomatized by subducted sediments-related melts and fluids, and the resultant magmas experienced some degrees of fraction crystallization during their ascent.

(3) Considering available regional tectonic magmatic, and structure analysis data, we propose an active continental margin environment is the most viable tectonic setting for their generation.

Acknowledgements

We appreciate ZHANG Yiping, ZHANG Beihang and

ZHAO Heng for their help in the field work. This work is jointly supported by the National Key Research and Development Program of China from the Ministry of Science and Technology of China (No. 2017YFC0601301), the National Natural Science Foundation of China (41502214, 41230207 and 41572190), the Outlay Research Fund of Institute of Geology, Chinese Academy of Geological Sciences (J1706), the Strategic Priority Research Program (B) of the Chinese Academy of Sciences (XDB18020203), the CPSF-CAS Joint Foundation for Excellent Postdoctoral Fellows (Grant no.2015LH0049), the China Postdoctoral Foundation funded project(2016M590990), the Key Research Program of Frontier Sciences, CAS (QYZDJ-SSW-SYS012), and China Geological Survey (12120115069601). This is a contribution to IGCP 592.

Manuscript received May 16, 2018
accepted Aug. 5, 2018
associate EIC YANG Jingsui
edited by FEI Hongcai

References

Barbrin, B., 1999. A review of the relationships between granitoid types, their origins and their geodynamic environments. Lithos, 46: 605–26.

Chappell, B.W., and White, A.J.R., 1974. Two contrasting granite types. Pacific Geology, 8: 173–174.

Chappell, B.W., and White, A.J.R., 1992. I- and S-type granites in the Lachlan Fold Belt. Transactions of the Royal Society of Edinburgh Earth Sciences, 83: 1–26.

Chen, B., Jahn, B. M., Wilde, S. and Xu, B., 2000. Two contrasting paleozoic magmatic belts in northern Inner Mongolia, China: petrogenesis and tectonic implications. Tectonophysics 328, 157–182.

Choi, S.G., Rajesh, V.J., Seo, J., Park, J.W., OH, C.W., Pak, S.J., and Kim, S.W., 2009. Petrology, geochronology and tectonic implications of Mesozoic high Ba-Sr granites in the Haemi area, Hongseong Belt, South Korea. Island Arc, 18: 266–281.

Conticelli, S., Avanzinelli, R., Ammannati, E., and Casalini, M., 2015. The role of carbon from recycled sediments in the origin of ultrapotassic igneous rocks in the Central Mediterranean. Lithos, 232: 174–196.

Dan, W., Li, X.H., Guo, J.H., Liu, Y., and Wang, X.C., 2012. Paleoproterozoic evolution of the eastern Alxa Block, westernmost North China: evidence from in situ zircon U–Pb dating and Hf–O isotopes. Gondwana Research, 21: 838–864.

Dan, W., Li, X.H., Wang, Q., Wang, X.C., Wyman, D.A., and Liu, Y., 2016. Phanerozoic amalgamation of the Alxa Block and North China Craton: Evidence from Paleozoic granitoids, U–Pb geochronology and Sr–Nd–Pb–Hf–O isotope geochemistry. Gondwana Research, 32: 105–121.

Defant, M.J., and Drummond, M.S., 1990. Derivation of some modern arc magmas by melting of young subducted lithosphere. Nature, 347: 662–665.

De La Roche, H., Leterrier, J., Grandclaude, P., and Marchal, M., 1980. A classification ofvolcanic and plutonic rocks using R1R2-diagram and major-element analyses: Itsrelationships with current nomenclature. Chemical Geology, 29: 183–210.

Drummond, M.S., and Defant, M.J., 1990. A model for trondhjemite–tonalite–dacite genesis and crustal growth via slab melting: Archaean to modern comparisons. Journal of Geophysical Research, 95: 21503–21521.

Dong, C.Y., Liu, D.Y., Li, J.J., Wan, Y.S., Zhou, H.Y., Li, C.D., Yang, Y.H. and Xie, L.W., 2007. Paleoproterozoic Khondalite Belt in the western North China Craton: new evidence from SHRIMP dating and Hf isotope composition of zircons from metamorphic rocks in the Bayan UI–Helan Mountains area. Chinese Science Bulletin, 52: 2984–2994.

Feng, J., Xiao, W., Windley, B., Han, C., Wan, B., Zhang, J.e., Ao, S., Zhang, Z., and Lin, L., 2013. Field geology, geochronology and geochemistry of mafic–ultramafic rocks from Alxa, China: Implications for Late Permian accretionary tectonics in the southern Altaids. Journal of Asian Earth Sciences, 78: 114–142.

Fowler, M.B., Henney, P.J., Darbyshire, D.P.F., and Greenwood, P.B., 2001. Petrogenesis of high Ba-Sr granites: the Rogart pluton, Sutherland. Journal of Geological Society of London, 158: 521–534.

Fowler, M.B., Kocks, H., Darbyshire, D.P.F. and Greenwood, P.B., 2008. Petrogenesis of high Ba–Sr plutons from the Northern Highlands Terrane of the BritishCaledonianProvince. Lithos, 105: 129–148.

Fowler, M.B., and Rollinson, H., 2012. Phanerozoic sanukitoids from Caledonian Scotland: implications for Archean subduction. Geology, 40 (12): 1079–1082.

Frost, B.R., Barnes, C.G., Collins, W.J., Arculus, R.J., Ellis, D.J., and Frost, C.D., 2001. A geochemical classification for granitic rocks. Journal of Petrology, 42: 2033–2048.

Geng, Y.S., Wang, X.S., Wu, C.M., and Zhou, X.W., 2010. Late-Paleoproterozoic tectonothermal events of the metamorphic basement in Alxa area: evidence from geochronology. Acta Petrologica Sinica, 26: 1159–1170 (in Chinese with English abstract).

Geng Yuansheng and Zhou Xiwen. 2012. Early Permian magmatic events in the Alxa metamorphic basement: Evidence from geochronology. Aca Petrologica Sinica, 28 (9):2667–2685 (in Chinese with English abstract).

Gong, J.H., Zhang, J.X., Wang, Z.Q., Yu, S.Y., Li, H.K., and Li, Y.S., 2016. Origin of the Alxa Block, western China: New evidence fromzircon U–Pb geochronology and Hf isotopes of the Longshoushan Complex. Gondwana Research, 36: 359–375.

Gong, J.H., Zhang, J.X., Wang, Z.Q., Yu, S.Y., Wang, D.S., and Zhang, H., 2017. Zircon U-Pb Dating, Hf Isotopic and Geochemical Characteristics of Two Suites of Gabbros in the Beidashan Region, Western Alxa Block:Its Implications for Evolution of the Central Asian Orogenic Belt. Acta Petrologica Sinica, 92(7): 1369–1388 (in Chinese with English abstract).

Gong, W.B., Hu, J.M., Wu, S.J., Liu, Y., and Zhao, Y.F., 2017. Deformation characteristics, timing and significance of the Langshan sinstral strike-slip ductile shear zone in Inner Mongolia. Earth Science Frontier, 24(3): 263–275 (in Chinese with English abstract).

Hildreth,W., and Moorbath, S., 1988. Crustal contributions to arc magmatism in the Andes of Central Chile. Contributions to Mineralogy and Petrology, 98: 455–489.

Hou, K.J., Li, Y.H., Zou, T.N., Qu, X.M., Shi, Y.R., and Xie, G.Q., 2007. Laser ablation-MC-ICP-MS technique for Hf isotope microanalysis of zircon and its geological applications. Acta Petrologica Sinica, 23: 2595–2604 (in Chinese with English abstract).

Hu, J.M., Gong, W.B., Wu, S.J., Liu, Y., and Liu, S.C., 2014. LA -ICP-MS zircon U–Pb dating of the Langshan Group in the northeast margin of the Alxa block, with tectonic implications. Precambrian Research, 255: 756–770.

Ishizuka, O., Taylor, R.N., Milton, J.A., and Nesbitt, R.W., 2003. Fluid–mantle interaction in anintra-oceanic arc: constraints from high-precision Pb isotopes. Earth and Planetary Science Letters, 211: 221–236.

Jahn, B. M., Wu, F. Y., and Hong, D. W., 2000. Important crustal growth in the Phanerozoic: Isotopic evidence of granitoids from east-central Asia. Journal of Earth System Science, 109: 5–20.

Jiang, X.Y., and Li, X.H., 2014. In situ zircon U–Pb and Hf–O isotopic results for ca. 73 Ma granite in HainanIsland: Implications for the termination of an Andean-type active continental margin in southeast China. Journal of Asian Earth Sciences, 82: 32–46.

Kamber, B.S., and Collerson, K.D., 2000. Role of “hidden” deeply subducted slabs in mantle depletion. Chemical Geology, 166: 241–254.

Kovalenko, V. I., Yarmolyuk, V. V., Kovach, V. P., Kotov, A. B., Kozakov, I. K., Salnikova, E. B., and Larin, A. M., 2004.

Isotope provinces, mechanisms of generation and sources of the continental crust in the Central Asian mobile belt: geological and isotopic evidence. Journal of Asian Earth Sciences, 23: 605–627.

La Flèche, M.R., Camire, G., and Jenner, G.A., 1998. Geochemistry of post-Acadian, Carboniferous continental intraplate basalts from the MaritimesBasin, Magdalen islands, Quebec, Canada. Chemical Geology, 148: 115–136.

Li,J.Y., Zhang, J., and Qu, J.F., 2012. Amalgamation of North China Craton with Alxa Block in the late of Early Paleozoic: evidence from sedimentary sequences in the NiushouMountain, Ningxia Hui Autonomous Region, NW China. Geological Review, 58: 208–214 (in Chinese with English abstract).

Li, X.H., 1997. Geochemistry of the Longshengophiolite from the southern margin of Yangtze Craton, SE China. Journal of Geochemistry, 31: 323–337.

Lin, L., Xiao, W., Wan, B., Windley, B., Ao, S., Han, C., Feng, J., Zhang, J., and Zhang, Z., 2014. Geochronologic and geochemical evidence for persistence of south-dipping subduction to late Permian time, Langshan area, Inner Mongolia (China): Significance for termination of accretionary orogenesis in the southern Altaids. American Journal of Science, 314: 679–703.

Liu, M., Zhang, D., Xiong, G.Q., Zhao, H.T., Di, Y.J., Wang, Z., and Zhou, Z.G., 2016a. Zircon U–Pb age, Hf isotope and geochemistry of Carboniferousintrusions from the Langshan area, Inner Mongolia: Petrogenesisand tectonic implications. Journal of Asian Earth Sciences, 120: 139–158.

Liu, Q., Zhao, G.C., Sun, M., Han, Y.G., Eizenhöfer, P.R., Zhang, X.R., Hou, W.Z., Zhu, Y.L.,Wang, B., Liu, D.X., and Xu, B., 2016b. Early Paleozoic subduction processes of the Paleo-Asian Ocean: insights from geochronology and geochemistry of Paleozoic plutonsin the Alxa Terrane. Lithos, 262: 546–560.

Liu, Z., Liao, S.Y., Wang, J.R., Ma,Z., Liu,Y.X., Wang, D.B., Tang, Y., and Yang, J., 2017. Petrogenesis of late Eocene high Ba-Sr potassic rocks from western Yangtze Block, SE Tibet: A magmatic response to the Indo-Asian collision. Journal of Asian Earth Sciences, 135: 95–109.

Lu, S.N., Yang, C.L., Li, H.K., and Li, H.M., 2002. A group of rifting events in the terminal Paleoproterozoic in the North China Craton. Gondwana Research, 5: 123–131.

Ludwig, K.R., 2003. User's Manual for Isoplot 3.0: A Geochronological, Toolkit for Microsoft Excel Berkeley Geochronology Center. special publication, 4: 1–71.

Malyshev, S.V., Khudoley, A.K., Prokopiev, A.V., Ershova, V.B., Kazakova, G.G., and Terentyeva, L.B., 2016. Source rocks of Carboniferous-Lower Cretaceous terrigenous sediments of the northeastern Siberian Platform: results of Sm -Nd isotope-geochemical studies. Russian Geology and Geophysics, 57: 421–433.

Maniar, P.D., and Piccoli, P.M., 1989. Tectonic discrimination of granitoids. Bulletin of the Geological Society of America, 101: 635–643.

Peccerillo, A., and Taylor, S.R., 1976. Geochemistry of Eocene calc-alkaline volcanic rocks from the Kastamonu area, northern Turkey. Contributions to Mineralogy and Petrology, 58: 63–81.

Peng, T.P., Wilde, S.A., Fan, W.M., and Peng, B.X., 2013. Late Neoarchean potassic highBa-Sr granites in the Taishan granite -greenstone terrane: petrogenesis and implications for continental crustal evolution. Chemical Geology, 344: 23–41.

Plank, T., and Langmuir, C.H., 1998. The geochemical composition of subducting sediment and its consequences for the crust and mantle. Chemical Geology, 145: 325–344.

Plank, T., 2005. Constraints from thorium/lanthanum on sediment recycling at subduction zones and the evolution of the continents. Journal of Petrology, 46 (5): 921–944.

Qian, Q., Chung, S.L., Lee, T.Y., and Wen, D.J., 2003. Mesozoic high-Ba-Sr granitoids from North China: geochemical characteristics and geological implications. Terra Nova, 15: 272–278.

Wang, T.Y., Wang, S.Z., and Wang, J.R., 1994. The Formation and Evolution of Paleozoic Continental Crust in Alxa Region. Lanzhou: Lanzhou University Press, 1–215 (in Chinesewith English abstract).

Wang, T.Y., Zhang, M.J., Wang, J.R., and Gao, J.P., 1998. The characteristics and tectonic implications of the thrust belt in Eugerwusu, China. Scientia Geologica Sinica, 33: 385–394 (in Chinesewith English abstract).

Wang, Z.Z., Han, B.F., Feng, L.X., and Liu, B., 2015. Geochronology, geochemistry andorigins of the Paleozoic–Triassic plutons in the Langshan area, western InnerMongolia, China. Journal of Asian Earth Sciences, 97: 337–351.

Watkins, J., Clemens, J., and Treloar, P., 2007. Archaean TTGs as sources of younger graniticmagmas: melting of sodic metatonalites at 0.6–1.2 GPa. Contributions to Mineralogy and Petrology, 154: 91–110.

Wiedenbeck, M., Alle, P., Corfu, F., Griffin, W.L., Meier, M., Oberli, F., Vonquadt, A., Roddick, J.C., and Speigel, W., 1995. Three natural zircon standards for U–Th–Pb, Lu–Hf, trace-element and REE, analyses. Geostandards Newsletter, 19: 1–23.

Windley, B.F., Alexeiev, D., Xiao, W.J., Kröner, A., and Badarch, G., 2007. Tectonic models for accretion of the Central Asian Orogenic Belt. Journal of the Geological Society of London, 164: 31–47.

Wu, T.R., and He, G.Q., 1993. Tectonic units and their fundamental characteristics on the northern margin of the Alxa block. Acta Geologica Sinica (English Edition), 67(4): 373–385.

Sláma, J., Košler, J., Condon, D.J., Crowley, J.L., Gerdes, A., Hanchar, J.M., Horstwood, M.S.A, Morris, G.A., Nasdala, L., Norberg, N., Schaltegger, U., Schoene, B., Tubrettk, M.N., and Whitehouse, M.J., 2008. Plešovice zircon—A new natural reference material for U–Pb and Hf isotopic microanalysis. Chemical Geology, 249: 1–35.

Schiano, P., Monzier, M., Eissen, J.P., Martin, H., and Koga, K.T., 2010. Simple mixing as the major control of the evolution of volcanic suites in the ecuadorian andes. Contributions to Mineralogy and Petrology, 160(2): 297–312.

Scholl, D.W., and Huene, R.V., 2007. Crustal recycling at modern subduction zones applied to the past–Issues of growth and preservation of continental basement crust, mantle geochemistry, and supercontinent reconstruction. Memoir of the Geological Society of America, 200: 9–32.

Schwindinger, M., and Weinberg, R., 2017. A felsic MASH zone of crustal magmas—Feedback between granite magma intrusion and in situ crustal anatexis. Lithos, 284–285: 109–121.

Sengör, A. M. C., Natal'in, B. A., and Burtman, V.S., 1993. Evolution of the Altaid tectonic collage and Palaeozoic crustal growth in Eurasia. Nature, 364: 299–307.

Spandler, C., and Pirard, C., 2013. Element recycling from subducting slabs to arc crust: a review. Lithos, 170–171: 208–223.

Su, H.M., Jiang, S.Y., Zhang, D.Y., and Wu, X.K., 2017. Partial Melting of Subducted Sediments Produced Early Mesozoic Calc-alkaline Lamprophyres from Northern Guangxi Province, South China. Scientific Reports, 7(1): DOI:10.1038/s41598-017-05228-w.

Sun, S.S., and McDonough, W.F., 1989. Chemical and isotopic systematics of oceanic basalts: Implications for mantle composition and processes. In: Saunders, A.D., Norry, M.J. (Eds.), Implications for Mantle Composition and Processes, Magmatism in the Ocean Basins. Geological Society, London, Special publication, 42: 313–345.

Sun, Y., Ying, J.F., Zhou, X.H., Shao, J.A., Chu, Z.Y., and Su, B.X., 2014. Geochemistry of ultrapotassic volcanic rocks in XiaoguliheNEChina: implications for the role of ancient subducted sediments. Lithos, 208: 53–66.

Tarney, J., and Jones, C.E., 1994. Trace element geochemistry of orogenic igneous rocks and crustal growth models. Journal of the Geological Society of London, 151: 855–868.

Tatsumi, Y., 2006. High-Mg andesites in the Setouchi volcanic belt, southwestern Japan: analogy to Archean magmatism and continental crust formation? Annual Reviews of Earth and Planetary Science Letters, 34: 467–499.

Todd, E., Gill, J.B., Wysoczanski, R.J., Handler, M.R., Wright,

I.C., and Gamble, J.A., 2010. Sources of constructional cross-chain volcanism in the southern Havre Trough: new insights from HFSE and REE concentration and isotope systematics. Geochemistry, Geophysics, Geosystems, 11(4): DOI:10.1029/2009gc002888.
Xiao, W., Han, C., Liu, W., Wan, B., Zhang, J.e., Ao, S., Zhang, Z., Song, D., Tian, Z., and Luo, J., 2014. How many sutures in the southern Central Asian Orogenic Belt: Insights from East Xinjiang–West Gansu (NW China)? Geoscience Frontiers, 5: 525–536.
Xiao, W.J., Windley, B.F., Sun, S., Li, J.L., Huang, B.C., Han, C.M., Yuan, C., Sun, M. and Chen, H.L., 2015. A tale of amalgamation of three Permo-Triassic collage systems in Central Asia: Oroclines, sutures, and terminal accretion. Annual Review of Earth and Planetary Sciences, 43: 477–507.
Xiao, W., Windley, B.F., Han, C., Liu, W., Wan, B., Zhang, J.E., Ao, S., Zhang, Z., and Song, D., 2018. Late Paleozoic to early Triassic multiple roll-back and oroclinal bending of the Mongolia collage in Central Asia. Earth-Science Reviews, 186: 94–128.
Xie, L., Yin, H.Q., Zhou, H.R., and Zhang, W.J., 2014. Permian radiolarians from the Engeerwusu suture zone in Alashan area, Inner Mongolia and its geological significance. Geological Bulletin of China, 33: 691–697 (in Chinese with English abstract).
Ye, H.M., Li, X.H., Li, Z.X., and Zhang, C.L., 2008. Age and origin of high Ba–Sr appinite–granites at the northwestern margin of the Tibet Plateau: implications for earlyPaleozoic tectonic evolution of the Western Kunlun orogenic belt. Gondwana Research,13: 126–138.
Yuan, W., and Yang, Z., 2015. The Alashan Terrane did not amalgamate with North China block by the Late Permian: evidence from Carboniferous and Permian paleomagnetic results. Journal of Asian Earth Sciences, 104: 145–159.
Zhang, C., Liu, L., Santosh, M., Luo, Q., and Zhang, X. 2016. Sediment recycling and crustal growth in the Central Asian Orogenic Belt: evidence from Sr–Nd–Hf isotopes and trace elements in granitoids of the Chinese Altay. Gondwana Research, 47: 142–160.
Zhang, J., Li, J.Y., Liu, J.F., Li, Y.F., Qu, J.F., and Feng, Q.W., 2012. The relationship between the Alxa Block and the North China Plate during the Early Paleozoic: New information from the Middle Ordovician detrial zircon ages in the eastern Alxa Block. Acta Petrologica Sinica, 28 (9): 2912–2934(in Chinese with English abstract).
Zhang, J., Li, J.Y., Xiao, W.X., Wang, Y.N., and Qi, W.H., 2013a. Kinematics and geochronology of multistage ductile deformation along the eastern Alxa block, NW China: new constraints on the relationship between the North China Plate and the Alxa block. Journal of Structural Geology, 57: 38–57.
Zhang, J.X., Gong, J.H., Yu, S.Y., Li, H.K., and Hou, K.J., 2013b. Neoarchean–Paleoproterozoic multiple tectonothermal events in the western Alxa block, North China Craton and their geological implication: evidence from zircon U–Pb ages and Hf isotopic composition. Precambrian Research, 235: 36–57.
Zhang, P., Wang, G.C., Li, Y.T., Zhang, S.Y., Peng, C., Zhao, H.W., Zha, Y.L., 2017. Emplacement Mechanism of the Akebasitao Pluton: Implications for Regional Tectonic Evolution of West Junggar, NW China. Acta Geologica Sinica (English Edition), 91(3): 857–874.
Zhang, S.H., Zhao, Y., Song, B., Yang, Z.Y., Hu, J.M., and Wu, H., 2007. Carboniferous granitic plutons from the northern margin of the North China Block: implications for a Late Paleozoic active continental margin. Journal of Geological Society of London, 164: 451–463.
Zhang, S.H., Zhao, Y., Song, B., Hu, J.M., Liu, S.W., Yang, Y.H., Chen, F.K., Liu, X.M., and Liu, J., 2009. Contrasting Late Carboniferous and Late Permian–Middle Triassic intrusive suites from the northern margin of the North China Craton: geochronology, petrogenesis and tectonic implications. Geological Society of America Bulletin, 121: 181–200.
Zhang, S.H., and Zhao, Y., 2013. Mid-crustal emplacement and deformation of plutons in an Andean-style continental arc along the northern margin of the North China Block and tectonic implications. Tectonophysics, 608: 176–195.
Zhang, Y.Y., Sun, M., Yuan, C., Xu, Y.G., Long, X.P., Tomurhuu, D., Wang, C.Y., and He, B., 2015. Magma mixing origin for high Ba–Sr granitic pluton in the Bayankhongor area, central Mongolia: Response to slab roll-back. Journal of Asian Earth Sciences, 113: 353–368.
Zhang, Z.J., Cheng, Q.M., Yao, L.Q., Bai, H.S., and Li, C., 2016. Zircon U-Pb-Hf Isotopic Systematics and Geochemistry of the Granites in the Wurinitu Molybdenum Deposit, Inner Mongolia, China: Implications for Tectonic Setting and Genetic Type of Mineralization. Acta Geologica Sinica (English Edition), 90(6): 2066–2079.
Zhao, G.C., Sun, M., Wilde, S.A., and Li, S.Z., 2005. Late Archean to Paleoproterozoic evolution of the North China Craton: key issues revisited. Precambrian Research, 136: 177–202.
Zheng, R.G., Wu, T.R., Zhang, W., Xu, C., Meng, Q.P., and Zhang, Z.Y., 2014. Late Paleozoic subduction system in the northern margin of the Alxa block, Altaids: geochronological and geochemical evidences from ophiolites. Gondwana Research, 25: 842–858.
Zheng, R.G., Li, J.Y., Xiao, W.J., Liu, J.F., and Wu, T.R., 2016. Discovery of Silurian Pluton in the Enger Us Region in the Northern Margin of Alxa Block. Acta Geologica Sinica, 90: 1725–1736 (in Chinese with English abstract).
Zheng, R.G., Li, J.Y., and Liu, J., 2017. The age of volcanic rocks of Amushan Formation on the northern margin of Alxa block: evidence from zircon U–Pb data. Geology in China, 44 (3): 612–613 (in Chinese with English abstract).

About the first and corresponding author

ZHENG Rongguo, male, Ph.D., graduated from the Peking university; research assistant of Institute of Geology, Chinese Academy of Geological Sciences. He is now interested in the Paleozoic tectonic evolution of the southern Central Asian Orogenic Belt. E-mail: rgzheng@163.com; Phone: 010-57909091